OXYGEN CHEMISTRY IN THE CIRCUMSTELLAR ENVELOPE OF THE CARBON-RICH STAR IRC+10216

MARCELINO AGÚNDEZ AND JOSÉ CERNICHARO

Departamento de Astrofísica Molecular e Infrarroja, Instituto de Estructura de la Materia, CSIC, Serrano 121, E–28006 Madrid, Spain

Draft version December 26, 2007

ABSTRACT

In this paper we study the oxygen chemistry in the C-rich circumstellar shells of IRC+10216. The recent discoveries of oxygen bearing species (water, hydroxyl radical and formaldehyde) toward this source challenge our current understanding of the chemistry in C-rich circumstellar envelopes. The presence of icy comets surrounding the star or catalysis on iron grain surfaces have been invoked to explain the presence of such unexpected species. This detailed study aims at evaluating the chances of producing O–bearing species in the C-rich circumstellar envelope only by gas phase chemical reactions. For the inner hot envelope, it is shown that although most of the oxygen is locked in CO near the photosphere (as expected for a C/O ratio greater than 1), some stellar radii far away species such as H_2O and CO_2 have large abundances under the assumption of thermochemical equilibrium. It is also shown how non-LTE chemistry makes very difficult the $CO \rightarrow H_2O$, CO_2 transformation predicted in LTE. Concerning the chemistry in the outer and colder envelope, we show that formaldehyde can be formed through gas phase reactions. However, in order to form water vapor it is necessary to include a radiative association between atomic oxygen and molecular hydrogen with a quite high rate constant. The chemical models explain the presence of HCO^+ and predict the existence of SO and H_2CS (which has been detected in a λ 3 mm line survey to be published). We have modeled the line profiles of H_2CO, H_2O, HCO^+, SO and H_2CS using a non-local radiative transfer model and the abundance profiles predicted by our chemical model. The results have been compared to the observations and discussed.

Subject headings: astrochemistry — circumstellar matter — molecular processes — stars: AGB and post-AGB — stars: individual(IRC+10216)

1. INTRODUCTION

IRC+10216 is a low mass AGB star losing mass at a rate of 2-4×10^{-5} $M_\odot$ yr^{-1} in the form of a molecular and dusty wind that produces an extended circumstellar envelope (CSE). The processes of dredge-up that occurs during this evolutionary late stage alter the elemental composition in the stellar surface (that is roughly solar, C/O<1, during the main sequence phase) resulting, in the case of IRC+10216, in a C/O ratio greater than 1, in what is known as a carbon star.

The physical conditions in the vicinity of the photosphere of an AGB star (typical temperatures of ∼2500 K and densities of ∼10^{14} cm^{-3}) make the material to be mainly molecular, with a composition determined by local thermodynamic equilibrium (LTE). It is now well established since the pioneering work of Tsuji (1973) that the C/O ratio completely determines the kind of chemistry taking place. The high stability of CO makes this molecule to have a large abundance locking almost all of the limiting reactant and allowing for the reactant in excess to form either carbon bearing molecules when C/O>1, and the opposite, i.e., oxygen bearing molecules, when C/O<1. This has been extensively confirmed by observations. A look to the list of molecules detected in IRC+10216 confirms that they are mostly carbon bearing species (see table 1 in Cernicharo et al. 2000 and §3). The only oxygen bearing molecule in C-rich AGB stars with a significant abundance, apart from CO, is SiO (Morris et al. 1975).

However, some other O–bearing molecules such as

Electronic address: marce, cerni@damir.iem.csic.es

H_2O (Melnick et al. 2001; Hasegawa et al. 2006), OH (Ford et al. 2003), and H_2CO (Ford et al. 2004) have recently been detected in IRC+10216. The existence of such molecules has been interpreted as the result of evaporation of cometary ices from a Kuiper belt analog in IRC+10216 (Ford & Neufeld 2001). The luminosity increase of the star, intrinsic to the red giant phase, would have caused the ice sublimation and subsequent release of water vapor to the gas phase in the circumstellar shells. OH would be produced when water is photodissociated by the interstellar UV field in the unshielded outer envelope and H_2CO would be the photodissociation product of an unknown parent molecule produced by sublimation of the ice mantles of these comets.

An alternative explanation has been proposed by Willacy (2004) in which H_2O would be produced through Fischer-Tropsch catalysis on the surface of iron grains, that would be present in the expanding envelope due to condensation from the gas phase of some fraction of the available iron. Fischer-Tropsch catalysis breaks the CO bond and produces H_2O and hydrocarbons such as CH_4.

O–bearing species have also been detected in the C-rich protoplanetary nebula CRL618 (Herpin & Cernicharo 2000). However, the production of these species has been interpreted by Cernicharo (2004) as the result of a rich photochemistry in a region of high density (∼10^7 cm^{-3}) and temperature (200-300 K) where large complex carbon-rich molecules are also produced (Cernicharo et al. 2001).

The aim of this paper is to investigate whether oxygen bearing molecules could be produced in the carbon-rich expanding gas of AGB stars by non-LTE mechanisms.

LTE calculations provide a good estimation of molecular abundances in the vicinity of the photosphere but as the gas expands the temperature and density decrease significantly and the chemical timescale increases, making chemical kinetics dominant in determining the molecular abundances. We describe the model of the circumstellar envelope in §2. The reaction network is discussed in §3. The results of the chemical model are presented in §4 together with comparisons of radiative transfer calculations with available observations. The conclusions are given in §5.

2. THE CIRCUMSTELLAR ENVELOPE

We assume spherical symmetry for the circumstellar envelope. In order to calculate the molecular abundances at different radii in the CSE, we follow the history of a volume element of gas with a given chemical composition travelling from the photosphere ($r=R_*$) to the end of the envelope ($r\sim10^{18}$ cm). We build a system of differential equations which integration yields the temporal evolution of the density of each gas species. The time has to be interpreted as radial position provided the gas travels outwards at a given velocity. Different processes are considered during this travel depending on the position in the CSE. Kinetic temperature (which determines the reaction rate constants) and total gas density radial profiles are needed to solve the system of equations. The values adopted for the different parameters used to model the CSE are given in table 1.

For model purposes the CSE is considered to consist of three different regions: the innermost region, the inner envelope, and the intermediate and outer envelope.

2.1. The innermost region

This zone corresponds to the region between the photosphere and r_0 (see Fig. 1a) . The adopted physical conditions are:

– The *temperature* is considered to vary as a power law of the radius r

$$T(r) = T_* \times \left(\frac{r}{R_*}\right)^{-\alpha} \qquad (1)$$

where T_* is the temperature at the photosphere and R_* is the star radius.

– The *density* profile is given by hydrostatic equilibrium. Considering the above temperature law, the gas density can be expressed as follows in terms of the value at r_0, $n(r_0)$

$$n(r) = n(r_0)\left(\frac{r}{r_0}\right)^{\alpha} exp\left\{-\frac{GM_*m_H\mu}{kT_*R_*^{\alpha}(1-\alpha)}\left(r_0^{(\alpha-1)}-r^{(\alpha-1)}\right)\right\} \qquad (2)$$

where k is the Boltzmann constant, G is the gravitational constant, M_* the mass of the star, m_H is the mass of a hydrogen atom and μ the mean molecular weight of gas.

The high densities and temperatures in this region allow to assume that molecular abundances are given by a LTE calculation.

2.2. The inner envelope

The gas travels from r_0 to r_c (see Fig. 1a), where r_c stands for condensation radius. At this distance, grain formation is supposed to occur. Radiation pressure on grains, together with momentum coupling of
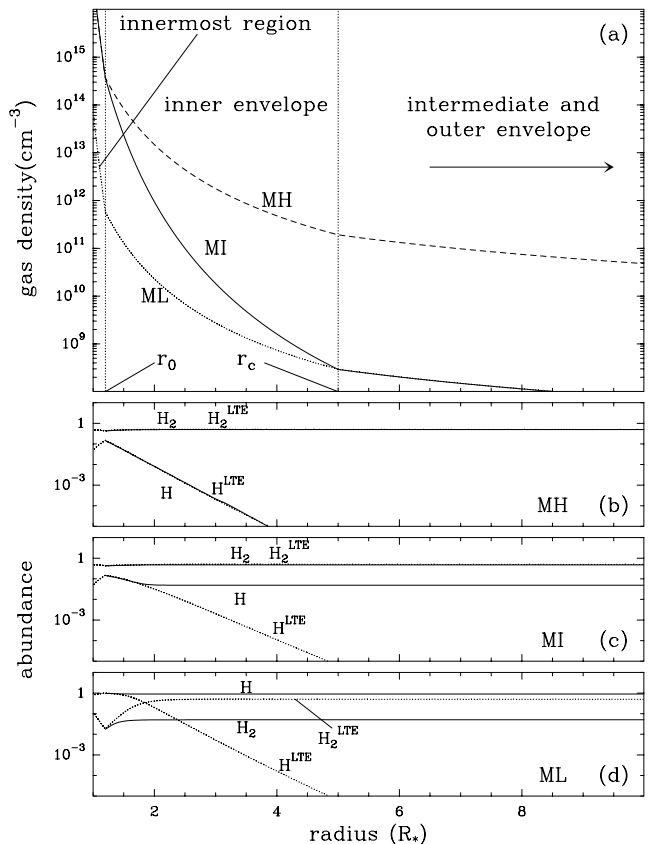

Fig. 1.— (a) Three different density profiles considered for the inner and innermost envelope: −**MH** [K_n=1, $n(r_0)$=3.7×10^{14} cm^{-3}], −**MI** [K_n=1.8565, $n(r_0)$=3.7×10^{14} cm^{-3}] and −**ML** [K_n=1, $n(r_0)$=1.2 × 10^{12} cm^{-3}]; all them use a r^{-2} law for r>r$_c$. (b), (c) and (d) show the abundances of H and H$_2$, relative to total number of hydrogen nuclei [n(H)+2n(H$_2$)], as given by LTE (dotted lines) and by chemical kinetics (solid lines) for the three density profiles: (b)→MH, (c)→MI and (c)→ML. Note the strong dependence of the H/H$_2$ ratio on the densities considered.

gas and grains, make the gas accelerate up to a terminal expansion velocity which remains constant beyond r_c. The mechanism responsible for the transport of the gas from r_0 to r_c is somewhat controversial. Hydrodynamical models (Bowen 1988) have shown that pulsational driven shocks can gradually move the gas up to r_c. Willacy & Cherchneff (1998) have applied this approach for modelling the chemistry in the inner envelope. An alternative mechanism could be that the gas close to the photosphere pulsates around an equilibrium position with an associated radial velocity very similar to the escape velocity. This could lead to a scenario in which shells of gas that are in levitation can eventually escape from the surroundings of the photosphere and some of them could reach r_c.

– The *temperature* profile in this region is given by equation 1.
– For the *density* profile we follow the treatment of a shocked extended region of a C-rich CSE of Cherchneff et al. (1992)

$$n(r) = n(r_0)exp\left\{-K_n\frac{GM_*m_H\mu(1-\gamma^2)}{kT_*R_*^{\alpha}(1-\alpha)}\left(r_0^{(\alpha-1)}-r^{(\alpha-1)}\right)\right\} \qquad (3)$$

where γ is defined in Cherchneff et al. (1992) and K_n is explained in the next paragraph.

The reference value $n(r_0)$ is not evident neither from observations nor from models. Previous models of the inner envelope of IRC+10216 (Cherchneff et al. 1992; Willacy & Cherchneff 1998) have used high values of $n(r_0)$ based on hydrodynamical models for periodically shocked Mira-like stars, which have density profiles as an output. However, with such high $n(r_0)$ values, the extrapolation to larger radii produces densities for the outer envelope much higher than those obtained from the law of conservation of mass, in which the absolute density is well determined by the mass loss rate and the expansion velocity (see equations 5 and 6 in §2.3). To reconcile the outer envelope density law with the high values in the inner regions we introduce the arbitrary factor K_n in equation 3. We consider three different density laws for the inner envelope, shown in Fig 1a, whose parameters $n(r_0)$ and K_n are given in table 1: MI (I for intermediate density); MH (H for high density), also considered for comparing our results with the previous model of Willacy & Cherchneff (1998) although it over-estimates the density for large radii; and finally ML (L for low density). We point out that the chemical time scale strongly depends on the density and also the H/H_2 ratio is completely different in a low or high density situation (see Figs. 1b, 1c and 1d). We will comment this in §4.1.

Another issue is how the gas travels from r_0 to r_c. As discussed above, different mechanisms could be operating. The simplest assumption to model the chemistry is to consider that the gas travels at constant velocity in this inner envelope. When using this approach we will assume a velocity of 1 km/s.

– *SiO condensation onto SiC grains.* Considering non-LTE effects, we investigated whether deposition of Si species (that are specially refractory) on SiC grains could affect the oxygen chemistry because SiO is the second more abundant O–bearing molecule. The scheme for grain formation in IRC+10216 could be as follows. The major type of grains are carbonaceous, most probably amorphous carbon (A.C.) as indicated by fitting the IR spectrum (Bagnulo et al. 1995). These grains would originate in condensation processes involving C_2H_2 (the most abundant C–bearing molecule after CO) that would take place at ~ 1000 K (~ 4 R_*). A minor type of grains would be SiC, as indicated by the 11.3 μm feature in the IR spectrum (Lorenz-Martins & Lefèvre 1993), that would condense at ~ 1500 K (~ 2 R_*). This condensation sequence is due to an inverse greenhouse effect in both types of grains (see McCabe 1982 for a theoretical approach and Frenklach et al. 1989 for experimental evidence). Although a more correct approach would be a chemical mechanism leading to the formation of grains from gaseous molecules, for our purposes we describe the condensation of SiC grains (A.C. grains are not considered because we are just interested in deposition of Si species on SiC grains) as a two-step process: (1) *nucleation* from SiC gas molecules in the context of homogeneous nucleation theory, which is basically described by the nucleation rate J_* (number of condensation nuclei formed per unit time and unit volume); and (2) *growth of grains* by accretion of gas phase molecules, that is described by the grain radius a_{gr}. The calculation of these two magnitudes is detailed
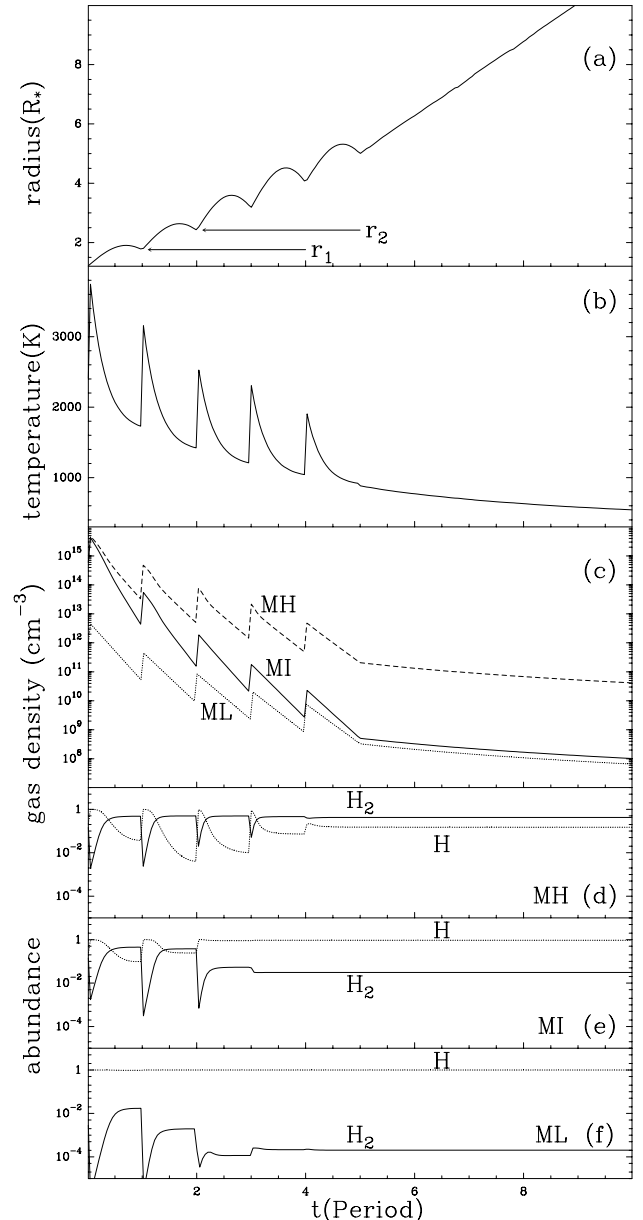

FIG. 2.— Parameters for a volume element of gas that suffers a history of 5 shocks: (a) trajectory; (b) temperature history; (c) density histories for models MH, MI and ML. (d), (e) and (f) show the H and H_2 abundances, relative to total number of hydrogen nuclei, calculated by chemical kinetics for the three density laws shown in (c).

in Appendix A.

– *Shocks.* An alternative to the mechanism of the gas travelling at constant velocity in the inner envelope is to consider the effect of gas driven by shocks. Molecular abundances are considerably affected by the steep changes in temperature and density associated to the shocks. We follow the approach of Willacy & Cherchneff (1998) but in a more simplistic way. The history of a volume element of gas to reach r_c from r_0 after a certain number of shocks is represented in Figs. 2a, 2b and 2c, and is described below . With one shock and subsequent relaxation, the gas moves from a position r_1 to r_2 ($r_2 > r_1$) following a harmonic trajectory. The gas in r_1 with temperature T_1 and density n_1 suffers a shock and we assume

TABLE 1
MODEL PARAMETERS

IRC+10216 parameters		Neutral molecules considered				Abundances relative to H_2 for parent species entering into the outer envelope		
[1]	R_*/cm	$6.5\ 10^{13}$	CH	H_2	N_2	SiH		H_2	
[2]	M_*/M$_\odot$	2	CH_2	O_2	NH	SiH_2	[18]	H	$4.5\ 10^{-3}$
[2]	r_0/R$_*$	1.2	CH_3	OH	NH_2	SiH_3	[10]	He	$2.0\ 10^{-1}$
[1]	r_c/R$_*$	5	CH_4	H_2O	NH_3	SiH_4	[7]	CO	$6.0\ 10^{-4}$
[1]	T_*/K	2320	C_2	HO_2	CN	Si_2	[19]	C_2H_2	$8.0\ 10^{-5}$
[3]	α	0.6	C_2H	H_2O_2	HCN	SiC	[19]	HCN	$4.9\ 10^{-5}$
[2]	$n(r_0)^{MH,MI}$/cm^{-3}	$3.7\ 10^{14}$	C_2H_2	CO	NS	SiCH	[10]	N_2	$8.0\ 10^{-5}$
	$n(r_0)^{ML}$/cm^{-3}	$1.2\ 10^{12}$	C_2H_3	CO_2	SH	$SiCH_2$	[13]	C_2H_4	$2.0\ 10^{-8}$
	$K_n^{MH,ML}$	1	C_2H_4	HCO	H_2S	SiC_2	[11]	CH_4	$3.5\ 10^{-6}$
	K_n^{MI}	1.8565	C_2H_5	H_2CO	CS	Si_2C	[11]	NH_3	$1.7\ 10^{-7}$
[4]	P/days	650	C_2H_6	CH_3O	HCS	SiN	[11]	SiH_4	$2.2\ 10^{-7}$
[3]	γ	0.89	C_3	CH_2OH	H_2CS	SiNH	[14]	H_2S	$6.0\ 10^{-10}$
[3]	$\mu(r<r_c)$/amu	1.7	C_3H	CH_3OH	S_2	SiO	[15]	CS	$1.2\ 10^{-7}$
[5]	v_{exp}/(km/s)	14.5	C_3H_2	HCCO	CS_2	SiO_2	[16]	SiS	$4.3\ 10^{-6}$
[6]	$\dot{M}$/(M$_\odot$ yr^{-1})	$3\ 10^{-5}$	C_4	NO	SO	SiS	[17]	SiC_2	$5.0\ 10^{-8}$
[7]	distance/pc	150	C_4H	NCO	SO_2		[11]	SiO	$8.0\ 10^{-7}$
[8]	$\tau_{1000}(r = 10^{16})$	12.7	C_4H_2		OCS				

REFERENCES. — [1] Ridgway & Keady 1988; [2] Willacy & Cherchneff 1998; [3] Cherchneff et al. 1992; [4] Witteborn et al. 1980; [5] Cernicharo et al. 2000; [6] Glassgold 1996; [7] Crosas & Menten 1997; [8] Doty & Leung 1998; [9] Rouleau & Martin 1991; [10] calculated according to LTE, solar elemental abundances and a C/O ratio of 2; [11] Keady & Ridgway 1993; [12] Wiedemann et al. 1991; [13] Goldhaber et al. 1987; [14] Abundance derived from the $1_{1,0}$-$1_{0,1}$ line of ortho-H_2S observed in Cernicharo et al. 2000 in the optically thin and LTE limit assuming T$_{rot}$ = 20 K and considering that H_2S is present for r>50 R$_*$; [15] Henkel et al. 1985; [16] Boyle et al. 1994; [17] upper limit by Gensheimer et al. 1995; [18] upper limit by Bowers & Knapp 1987; [19] Fonfría et al. 2006.

that the immediately post-shocked gas increases its temperature by a factor 2 and its density by a factor 10 (typical values obtained by Willacy & Cherchneff 1998 from hydrodynamical considerations). Then the gas relaxes its temperature and density exponentially until reaching the new radius r_2 (with temperature T_2 and density n_2) in a time interval equal to the period of pulsation of the star P. In this way the gas progressively moves outwards until reaching r_c, beyond which an expansion at constant velocity v_{exp} takes place.

In Fig. 2 we plot the trajectory, temperature and the three density laws introduced previously. Note that again the H/H_2 ratio strongly depends on the total gas density (see Figs. 2d, 2e and 2f).

2.3. The intermediate and outer envelope

It extends from r_c. The gas expands adiabatically at constant velocity v_{exp}. The molecules in the very outer envelope are no longer shielded by the dust of the CSE against the interstellar UV field, and are then photodissociated. Cosmic rays also play a role ionizing some species.

– The *temperature* profile is taken from the fit of Mamon et al. (1988) to the results of Kwan & Linke (1982) for the outer envelope of IRC+10216

$$T(r) = max\left[10, 14.6\left(\frac{r}{9 \times 10^{16}}\right)^{-p}\right] \quad (4)$$

where r is expressed in cm and p takes values of 0.72 for $r<9\times10^{16}$ and 0.54 for $r>9\times10^{16}$.

– The *density* profile is given by the law of conservation of mass:

$$\dot{M} = n(r)m_H\mu v_{exp}4\pi r^2 \quad (5)$$

which, with the values given in table 1 and assuming that

hydrogen is mostly molecular ($\mu\sim2$ amu), results in

$$n(r) = \frac{3.1 \times 10^{37}}{r(cm)^2} \quad cm^{-3} \quad (6)$$

– The photodissociation rate Γ_i for a molecule i at a radius r depends on the UV field at that radius:

$$\Gamma_i(r) = \int_{91.2}^{\lambda_i} 4\pi J_\lambda(r)\sigma_i(\lambda)d\lambda \quad (7)$$

where $4\pi J_\lambda(r)$ is the UV field at r in photons cm^{-2} s^{-1} nm^{-1}, $\sigma_i(\lambda)$ is the photodissociation cross section and the integral extends from 91.2 nm (Lyman cutoff) to a threshold value λ_i that depends on each molecule. The calculation of each $\Gamma_i(r)$ involves the knowledge of the cross section and the solution of the UV radiative transfer for calculating J_λ at each radius r, which will depend in a first approximation on the amount of dust that surrounds the point r. In practice, photodissociation rates are usually expressed in the literature (Le Teuff et al. 2000) for plane-parallel geometry as a function of the visual extinction A_v (in magnitudes) measured along the direction normal to the infinite plane

$$\Gamma_i(A_v) = A_i exp(-C_i A_v) \quad (8)$$

with specific parameters A_i and C_i for each molecule. For our purposes we have adopted this simple approach just correcting for the geometrical difference from plane-parallel to spherical. The procedure used for such correction as well as the resulting A_v radial profile are detailed in appendix B.

3. THE CHEMISTRY

We consider solar elemental abundances (oxygen from Allende Prieto et al. 2001 and the rest

from Cox 2000) and assume a C/O ratio of 2. The chemistry in IRC+10216 is dominated by carbon bearing molecules. For carbon chain radicals C_nH see Tucker et al. (1974); Thaddeus et al. (1985); Guélin et al. (1978); Cernicharo et al. (1986); Guélin et al. (1987a, 1997); Cernicharo & Guélin (1996). For carbon chain radicals C_nN see Wilson et al. (1971); Guélin & Thaddeus (1977); Guélin et al. (1998). For cyanopolyynes $HC_{2n+1}N$ see Morris et al. (1971, 1976); Winnewisser & Walmsley (1978); Bell et al. (1982). For sulfur–carbon chain molecules C_nS see Wilson et al. (1971); Cernicharo et al. (1987); Bell et al. (1993). And for silicon bearing molecules SiC_n see Cernicharo et al. (1989); Thaddeus et al. (1984); Apponi et al. (1999); Ohishi et al. (1989). However, since we are just interested in oxygen chemistry, in our model we don't include very long carbon chains but only the 65 neutral molecules given in table 1.

As initial abundances for the inner envelope we take those given by LTE at r_0, while for the outer shells we adopt initial abundances for some parent molecules taken from the literature or from a LTE calculation when no data are available (see table 1). This procedure is motivated by the processes occurring in the intermediate envelope (specially on grain surfaces) that presumably alter the molecular abundances (hydrides such as CH_4, NH_3, SiH_4 and H_2S are supposed to form via such processes).

Different types of reactions dominate the chemistry depending on the region of the CSE considered. The temperatures in the inner envelope are not high enough to make ions abundant but allow for reactions with activations energies of up to a few tens of thousands of K to occur. Therefore, important processes are termolecular reactions, its reverse (thermal dissociation) and bimolecular reactions between neutrals. The outer envelope chemistry is dominated by photodissociations, radical-molecule reactions without activation energy and radiative associations. Although all the species detected in IRC+10216, except HCO^+, are neutral, ionic chemistry is necessary to explain the formation of some species. Therefore, when modelling the chemistry in the outer envelope we add 80 ionic species (mainly the positive ions and protonated species of the neutral molecules of table 1) and include the subsequent reactions in which they are involved. The rate constants have been taken from different sources: databases such as NIST Chemical Kinetics Database[1], UMIST Database 1999 (Le Teuff et al. 2000) and osu.2003 Database (Smith et al. 2004); estimations for reactions involving S– and Si–bearing species from Willacy & Cherchneff (1998); combustion mechanisms such as GRI–Mech (Smith et al. 1999) or the one of A. Konnov (Konnov 2000); and from a revision of the last published data of rate constants for the type of reactions mentioned above. When no data are available for the whole temperature range studied here (10-4000 K) we have either extrapolated the expression or fixed the rate constant to its value at the nearest temperature for which it is known. When rate constants for reverse reactions were unknown or uncertain, detailed balance has been applied for calculating them from thermochem-

[1] The NIST Chemical Kinetics Database is available on the World Wide Web at http://kinetics.nist.gov/index.php.

TABLE 2
Reactions relevant for oxygen chemistry

Reaction	A	n	C
Important reactions in the INNER envelope			
R1 $H + H + H_2 \rightarrow H_2 + H_2$	8.6×10^{-33}	-0.60	0
R2 $H + H + H \rightarrow H_2 + H$	8.8×10^{-33}	0.00	0
R3 $H + H + He \rightarrow H_2 + He$	6.1×10^{-33}	-0.13	-39
R4 $H_2 + H_2 \rightarrow H + H + H_2$	8.4×10^{-09}	-0.24	52043
R5 $H_2 + H \rightarrow H + H + H$	8.6×10^{-09}	0.36	52043
R6 $H_2 + He \rightarrow H + H + He$	5.9×10^{-09}	0.23	52003
R7 $Si + CO \rightarrow SiO + C$	1.3×10^{-09}	0.00	34513
R8 $SiO + C \rightarrow Si + CO$	1.0×10^{-09}	-0.23	1291
R9 $C + H_2 \rightarrow CH + H$	3.1×10^{-10}	0.16	11894
R10 $OH + Si \rightarrow SiO + H$	1.0×10^{-10}	0.00	0
R11 $OH + H_2 \rightarrow H_2O + H$	2.2×10^{-12}	1.43	1751
R12 $SiO + CO \rightarrow CO_2 + Si$	4.2×10^{-13}	0.67	32225
R13 $CO_2 + H_2 \rightarrow H_2O + CO$	3.2×10^{-7}	1.53	56906
R14 $OH + CO \rightarrow CO_2 + H$	1.2×10^{-13}	0.95	-73 [a]
R15 $O + H_2 \rightarrow OH + H$	3.5×10^{-13}	2.60	3241
R16 $CO_2 + Si \rightarrow SiO + CO$	2.7×10^{-11}	0.00	282
Important reactions in the OUTER envelope			
R17 $O + NH_2 \rightarrow OH + NH$	1.2×10^{-11}	0.00	0
R18 $O + CH_3 \rightarrow H_2CO + H$	1.4×10^{-10}	0.00	0
R19 $OH + S \rightarrow SO + H$	6.6×10^{-11}	0.00	0
R20 $O + SH \rightarrow SO + H$	1.2×10^{-10}	0.00	-74 [c]
R21 $O + NH \rightarrow NO + H$	1.2×10^{-10}	0.00	0
R22 $CN + OH \rightarrow NCO + H$	1.4×10^{-10}	0.00	0
R23 $S + CH_3 \rightarrow H_2CS + H$	1.4×10^{-10}	0.00	0
R24 $O + OH \rightarrow O_2 + H$	1.8×10^{-11}	0.00	-175 [b]
R25 $O + CH_2 \rightarrow HCO + H$	5.0×10^{-11}	0.00	0
R26 $^{13}C^+ + {}^{12}CO \rightarrow {}^{12}C^+ + {}^{13}CO$	3.4×10^{-10}	-0.50	1.3
R27 $SiO + C^+ \rightarrow Si^+ + CO$	5.4×10^{-10}	0.00	0
R28 $H_2^+ + H_2 \rightarrow H_3^+ + H$	2.1×10^{-9}	0.00	0
R29 $H_3^+ + CO \rightarrow HCO^+ + H_2$	1.7×10^{-9}	0.00	0
R30 $HCO^+ + HCN \rightarrow CO + HCNH^+$	3.1×10^{-9}	0.00	0
R31 $HCO^+ + C_2H_2 \rightarrow CO + C_2H_3^+$	1.4×10^{-9}	0.00	0
R32 $SiS + C^+ \rightarrow SiS^+ + C$	2.3×10^{-9}	0.00	0
R33 $SiS^+ + H \rightarrow SH + Si^+$	1.9×10^{-9}	0.00	0
R34 $SiS + S^+ \rightarrow SiS^+ + S$	3.2×10^{-9}	0.00	0
R35 $SiO^+ + CO \rightarrow CO_2 + Si^+$	7.9×10^{-10}	0.00	0
R36 $O + H \rightarrow OH + h\nu$	9.9×10^{-19}	-0.38	0
R37 $S + CO \rightarrow OCS + h\nu$	1.6×10^{-17}	-1.50	0
R38 $HCO^+ + e^- \rightarrow CO + H$	1.1×10^{-7}	-1.00	0
R39 $H_3CS^+ + e^- \rightarrow H_2CS + H$	3.0×10^{-7}	-0.50	0
R40 $H_2CO^+ + e^- \rightarrow HCO + H$	1.0×10^{-7}	-0.50	0
R41 $SiO + h\nu \rightarrow Si + O$	1.0×10^{-10}	0.00	2.3
R42 $H_2O + h\nu \rightarrow OH + H$	5.9×10^{-10}	0.00	1.7
R43 $CH_4 + h\nu \rightarrow CH_3 + H$	2.2×10^{-10}	0.00	2.2
R44 $H_2 + CR \rightarrow H_2^+ + e^-$	1.2×10^{-17}	0.00	0
Reactions not considered in previous chemical models [d]			
R45 $O + H_2 \rightarrow H_2O + h\nu$	1.0×10^{-18}	0.00	0
R46 $HCO^+ + H_2 \rightarrow H_3CO^+ + h\nu$	5.0×10^{-15}	0.00	0

Note. — Rate constants for termolecular and bimolecular reactions are given by $k = A \times (T/300)^n \times \exp(-C/T)$, for photodissociations ($h\nu$) are given by $k = A \times \exp(-C\ A_v)$ while for reactions with cosmic rays (CR) are given by $k = A$. Units are $cm^6 s^{-1}$ for termolecular reactions, $cm^3 s^{-1}$ for bimolecular reactions and s^{-1} for photodissociations and reactions with cosmic rays.

[a] $k(T<80K) = k(T=80K)$
[b] $k(T<167K) = k(T=167K)$
[c] $k(T<298K) = k(T=298K)$
[d] See text for a discussion on these rate constants.

ical properties of the species involved. Photodissociation rates have been taken from the quoted databases when available, or assumed to be equal to those of similar molecules otherwise to ensure that all molecules are dissociated at some radius within the envelope. CO and H_2 are known to be affected by self-shielding against interstellar UV photons due to their large abundance. CO

N	Reaction	A	n	C	T_1	T_2	T_{range}	Ref
1	H + H + H2 <=> H2 + H2	8.640E-33	-0.60	0.00	50.	5000.	ALL__T	NIST
2	H + H + He <=> H2 + He	6.070E-33	-0.13	-39.00	77.	2000.	ALL__T	NIST
3	H + H + H <=> H2 + H	8.820E-33	0.00	0.00	50.	5000.	ALL__T	NIST
4	CH + He <=> C + H + He	3.160E-10	0.00	33704.00	2500.	3800.	LOW__T	NIST
5	CH + H2 <=> C + H + H2	8.830E-10	0.00	33704.00	2500.	3800.	LOW__T	NIST

NOTE. — The full version of table 3 is available in the electronic edition of the *Astrophysical Journal*.

photodisssociation rate as a function of radial position is taken from Doty & Leung (1998), who studied the CO case specifically for IRC+10216. For H_2 we use the same result correcting for the different unattenuated photodissociation rate.

The most important reactions for oxygen chemistry are shown in table 2 . Table 3 contains the complete set of reactions.

4. RESULTS AND DISCUSSION

4.1. *Oxygen chemistry in the inner envelope*

In this section we (i) first compare the results of chemical kinetics (assuming an expansion at constant velocity of 1 km s^{-1}) with those of chemical equilibrium, (ii) secondly we discuss the effects that SiO depletion from the gas phase could have on oxygen chemistry and (iii) finally we consider the chemistry with shocks.

(i) The densities considered in the inner envelope affect, among other parameters, the H/H_2 ratio. Figs. 1b, 1c and 1d show the H_2 and H abundances for models MH, MI and ML. The high densities of model MH make the chemical time scale to be lower than the dynamical time scale associated to an expansion at 1 km/s; therefore, reactions R1 to R6

$$R1, R2, R3 \qquad H + H + M \;\rightarrow\; H_2 + M$$
$$R4, R5, R6 \qquad H_2 + M \qquad\rightarrow\; H + H + M$$
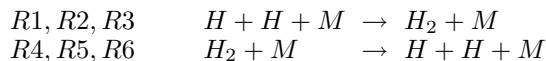
are rapid enough to produce LTE abundances for H and H_2. The steep decay in density of model MI makes that at $\sim$2 R$_*$ reactions R1 to R6 become too slow, so that the H abundance is frozen at a value of 5×10^{-2}. Both models MH and MI allow hydrogen to enter the intermediate shells and outer envelope mostly as H_2. Model MI has a low photospheric density and therefore hydrogen exists in atomic form rather than molecular. For larger radii the decrease in temperature makes molecular the most stable form. However, chemical kinetics does not allow for a H→H_2 transformation and hydrogen enters the outer envelope in atomic form. It is seen how both the density at the photosphere and the density radial profile affect the H/H_2 ratio. There are observational constraints about this ratio that suggest that hydrogen is mainly molecular in the CSE (based on an upper limit for the H_2 mass in the CSE and on an estimation of the H mass from observations of the 21 cm line, see discussion in Glassgold 1996). This suggests a high density scenario, such as the one of models MH or MI, for the inner envelope.

In what concerns oxygen chemistry, according to chemical equilibrium, for the densities and temperatures prevailing in the inner envelope, almost all the oxygen available in a C-rich gas is locked in CO, with SiO being 2-5 orders of magnitude less abundant. Any other O–bearing molecule has an LTE abundance always below $\sim$10^{-10}. But some stellar radii away from the photosphere, where the temperature has decreased below $\sim$700 K, the chemical system experiences a significant change and molecules such as H_2O and CO_2 become very abundant in LTE (see dotted lines in Figs. 3a, 3b and 3c). This is related to the fact that the most stable form for both carbon and oxygen is the CO molecule in a high temperature regime, whereas for a low temperature regime carbon is preferably locked in CH_4 and oxygen in H_2O (Tsuji 2000), as is easily seen from the analysis of the equilibrium constant of this reaction:

$$CO + 3H_2 \rightleftharpoons CH_4 + H_2O \qquad (9)$$
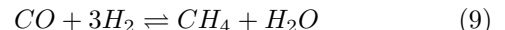
which can be fitted by the expression

$$K_{eq}(T) = 1.58 \times 10^{-50} \Big(\frac{T}{300}\Big)^{0.09} exp(24427/T) \quad (10)$$

for a temperature interval of 200-2000 K (K_{eq} with units of (molecules/cm^3)$^{-2}$). The formation of CH_4 and H_2O from CO and H_2 is exothermic and involves less particles, so according to Le Chatelier's principle the CH_4/H_2O mixture dominates over the CO/H_2 mixture at low temperatures and high densities. In our case, as temperature decreases so does density. Thus, a total CO→H_2O transformation is only produced for T$\lesssim$400 K (r$\gtrsim$ 18 R$_*$) in model MH (see Fig. 3a) and for larger radii in models MI and ML. Despite a total CO→H_2O transformation takes place beyond $\sim$20 R$_*$, the three models show a considerably increase in the LTE abundance of H_2O beyond $\sim$10 R$_*$.

In order to have LTE abundances in the inner envelope, the chemical time scale τ_{chem} has to be shorter than the dynamical time scale τ_{dyn} associated to the expansion for the gas being able to readapt its molecular abundances to the actual physical conditions (temperature and density) as it expands. The situation in the inner envelope of IRC+10216 is such that $\tau_{chem}<\tau_{dyn}$ in the vicinity of the photosphere, but as temperature and density fall with radial distance, chemical reactions become slower and for a certain radio (that depends on the chemical species) $\tau_{chem}>\tau_{dyn}$. There, molecular abundances "freeze" and the LTE scenario disappears.

The LTE abundance of CO remains constant from the photosphere to $\sim$20 R$_*$. Thus, whether chemical kinetics is rapid (LTE is reproduced) or slow ("freezing" effect) the CO abundance won't be modified. The situation is different for SiO (see Figs. 3a, 3b and 3c). Its LTE abundance at r_0 is $\sim$10^{-8} while at $\sim$3-5 R$_*$ it increases to $\sim$10^{-5}. For this abundance enhancement to occur as the gas expands, SiO has to take the oxygen from CO via reaction R7
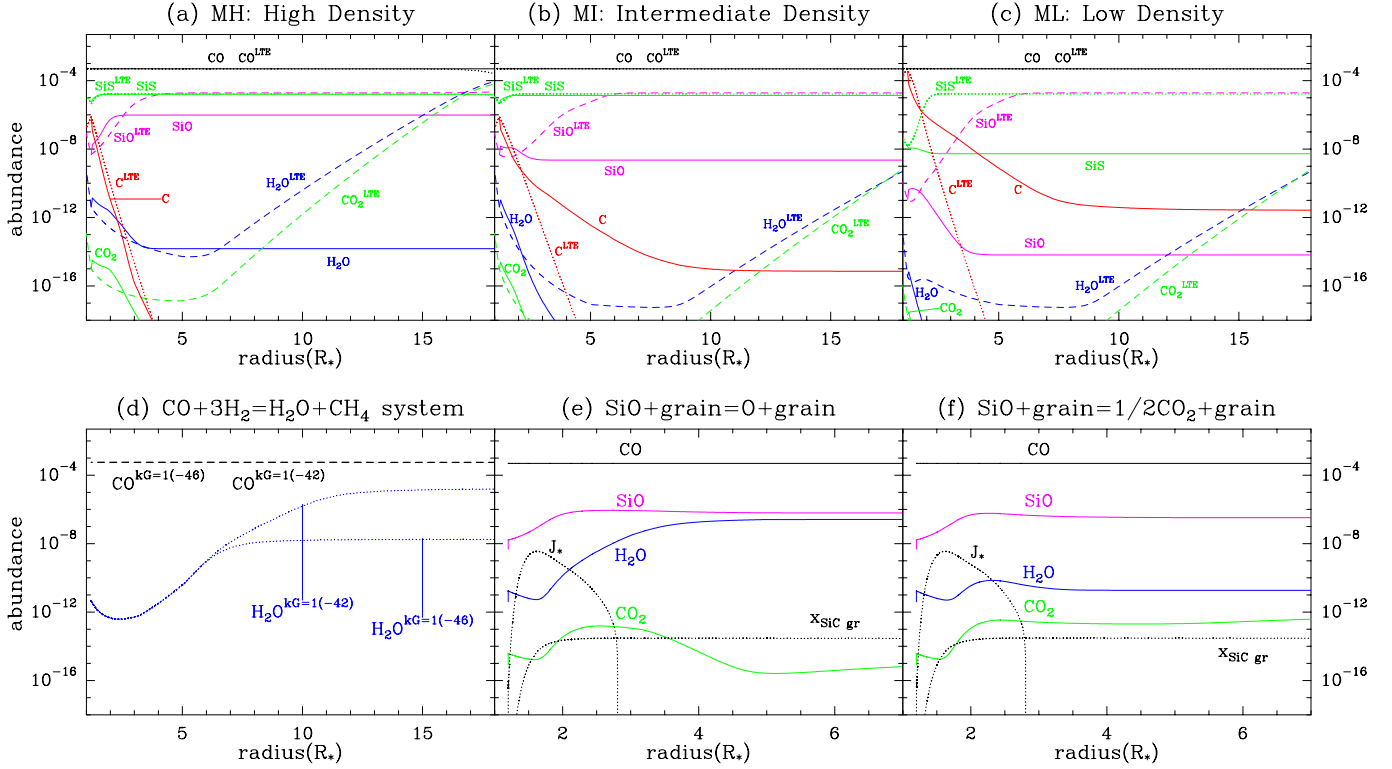
$$R7 \qquad Si + CO \;\rightarrow\; SiO + C$$

Fig. 3.— Abundances, relative to total number of hydrogen nuclei, of some oxygen bearing molecules. −(a), (b) and (c): abundances given by LTE (dotted and dashed lines) and by chemical kinetics (solid lines) assuming a constant velocity expansion of 1 km/s and the density profiles MH→(a), MI→(b) and ML→(c). −(d): abundances of CO and H_2O for a CO,H_2,CH_4,H_2O system with k_G (see text) equal to 10^{-42} and 10^{-46} cm^9 s^{-1}. −(e) and (f): abundances given by chemical kinetics with the density profile MH when we consider that 90% of SiO gas is deposited onto SiC grains and that the corresponding oxygen is released to the gas phase either as atomic oxygen→(e) or as CO_2→(f). The nucleation rate of SiC grains J_* (with units of nuclei cm^{-3} s^{-1}) and its abundance x_{SiCgr}, relative to total number of hydrogen nuclei, are also plotted as dotted lines. See the electronic edition of the Journal for a color version of this figure

which has a low rate and the above considerations about τ_{chem} and τ_{dyn} apply. Only high densities and/or low expansion velocities will make SiO reach this abundance of $\sim 10^{-5}$. For the three density models considered and the expansion velocity of 1 km/s assumed, only the MH model makes SiO reach an abundance near its LTE value, whereas MI and ML lead to a non-LTE situation in which SiO abundance remains low. The abundance of atomic C has a great impact on SiO. In models MI and ML it remains well above its LTE value while in MH it follows the decreasing LTE profile being destroyed by reaction R9

$$R9 \qquad C + H_2 \ \rightarrow \ CH + H$$
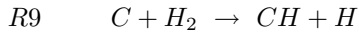
The H "freezing" effect of models MI and ML makes the reverse of reaction R9 to proceed at a higher rate that in a LTE situation making C overabundant which, through reaction R8
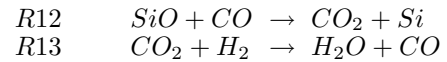
$$R8 \qquad SiO + C \ \rightarrow \ Si + CO$$
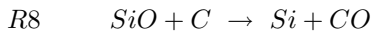
destroys SiO making it underabundant with respect to a LTE situation. Again a high density scenario is required for explaining the SiO observational abundance of 8×10^{-7} (estimated by Keady & Ridgway 1993 through IR ro-vibrational lines) that could be due either to this "freezing" effect or to depletion on SiC grains after reaching its LTE abundance of $\sim 10^{-5}$. Neither of the models run made any other O–bearing molecule to have a significant abundance. In this high temperature regime H_2O is related to SiO by two routes: (1) competition for OH
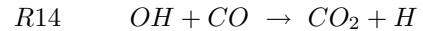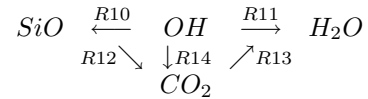
via reactions R10 and R11

$$R10 \qquad OH + Si \ \rightarrow \ SiO + H$$
$$R11 \qquad OH + H_2 \ \rightarrow \ H_2O + H$$
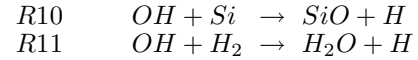
and (2) through CO_2, directly via reactions R12+R13

$$R12 \qquad SiO + CO \ \rightarrow \ CO_2 + Si$$
$$R13 \qquad CO_2 + H_2 \ \rightarrow \ H_2O + CO$$

or involving OH which is converted into CO_2 via reaction R14

$$R14 \qquad OH + CO \ \rightarrow \ CO_2 + H$$

The following scheme shows these relations:

$$SiO \ \overset{R10}{\underset{R12}{\longleftarrow}} \ OH \ \overset{R11}{\underset{R13}{\longrightarrow}} \ H_2O$$
$$\downarrow R14$$
$$CO_2$$

where the connection between the species is produced by the reactions shown above and also by their reverse processes, so we have a reversible system. Nevertheless, these mechanisms are not efficient in producing H_2O from SiO. For H_2O to take the oxygen from CO the chances are scarce because when the LTE abundance of H_2O increases, the temperatures (<700 K) make that the possible chemical routes for a CO→H_2O conversion will be too slow due to the large activation energy for breaking the CO bond. At this point, we would like to know if we miss some important reactions, rapid enough for allowing this CO→H_2O transformation in the conditions of the inner envelope of IRC+10216. We consider an scenario given by model MH (high density in order to

have a short τ_{chem}) and the chemical reaction given by equation 9. This reaction can be decomposed in several elementary reactions, for example

$$
\begin{array}{rl}
CO + H_2 \xrightarrow{k_S} CH + OH & (S) \\
OH + H_2 \longrightarrow H_2O + H & \\
CH + H_2 \longrightarrow CH_2 + H & \\
CH_2 + H_2 \longrightarrow CH_3 + H & \\
CH_3 + H_2 \longrightarrow CH_4 + H & \\
2 \times \quad H + H + H_2 \longrightarrow H_2 + H_2 & \\
\mathbf{CO + 3\,H_2} \xrightarrow{\mathbf{k_G}} \mathbf{CH_4 + H_2O} & \mathbf{(G)}
\end{array}
$$
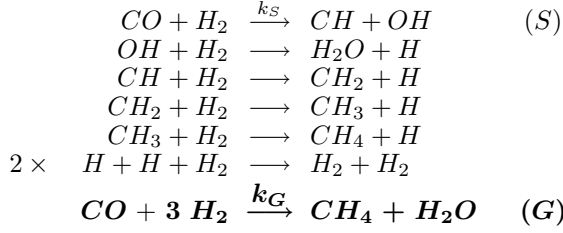
In any mechanism composed of elementary reactions, the rate of the global reaction (G) will be given by the rate of the slowest elementary reaction (S). In this case the slowest elementary step will be the break of the CO bond, since it has the largest activation barrier. The number of H_2O molecules produced or the number of CO molecules destroyed in the global reaction, per unit time and unit volume, is equal to the number of CO molecules destroyed in the slowest elementary reaction, per unit time and unit volume. We assign a rate constant k_G for the global reaction G, calculate the reverse rate constant via detailed balance, and run the model for a CO,H_2,CH_4,H_2O system in which only the global reaction G and its reverse operate. Then we vary k_G until some significant fraction of CO is transformed into H_2O and CH_4. Models for k_G equal to 10^{-42} and 10^{-46} cm^9 s^{-1} are shown in Fig. 3d. It is seen that above a threshold value of $\sim 10^{-44}$ cm^9 s^{-1} for k_G, the CO$\rightarrow$H$_2$O transformation is significant. The rate of destruction of CO molecules given by reaction G is $k_G \times x_{CO} \times n^4$ (x_{CO} is the CO abundance relative to H_2 and n is the density of H_2) while the rate of destruction of CO molecules by reaction S is $k_S \times x_{CO} \times n^2$. Since both rates have to be equal, we arrive to $k_S = k_G \times n^2$. Taking 10^{-44} for k_G and a density of 10^{10} cm^{-3} (roughly the value in the region 10-20 R$_*$ where the discussed process should take place) results in $k_S = 10^{-24}$ cm^3 s^{-1}. Therefore, we need a bimolecular reaction similar to reaction S with a rate constant greater than 10^{-24} cm^3 s^{-1} for temperatures lower than ~ 700 K. There is no data in the literature about a rate constant for a reaction such as S. Nevertheless, we can estimate an upper limit for k_S if we assume a maximum temperature independent value of 10^{-9} cm^3 s^{-1} for the reverse reaction and apply detailed balance. This results in activation energies of $\sim 80,000$ K for k_S, which for temperatures below 700 K imply rate constants well below 10^{-24} cm^3 s^{-1}. So we don't expect a chemical route that is able to convert CO into H_2O in the inner envelope within the gas phase and during an adiabatic expansion.

(ii) Such a CO$\rightarrow$H$_2$O process seems too slow, but there is another O–bearing molecule which locks some important amount of oxygen, i.e. SiO, which is expected to condense onto SiC grains. How could H_2O abundance be affected by *SiO condensation* during the expansion?. When we consider such a process in our model, H_2O abundance remains low. The reason is that, as explained above, H_2O is related to SiO in such a way that H_2O becomes abundant when SiO does, but not when SiO depletes. Then, we consider in model MH (where SiO is formed with a significant abundance) a speculative pro-

cess that can be summarized as follows: a SiO molecule condenses onto a SiC grain and the Si atom incorporates into the grain lattice while the O atom is released to the gas phase

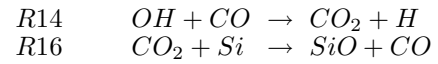$$SiO_{gas} + grain \rightarrow grain \cdots Si + O_{gas}$$
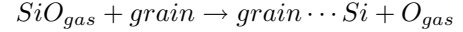
We assume that 90% of the SiO formed in the gas phase is deposited onto SiC grains and that all that oxygen, formerly contained in SiO, is released to the gas phase as atomic oxygen (see Fig. 3e). It is seen that molecules like H_2O and CO_2 increase their abundances. H_2O takes efficiently the oxygen when it is in atomic form via reactions R15+R11

$$
\begin{array}{lll}
R15 & O + H_2 & \rightarrow OH + H \\
R11 & OH + H_2 & \rightarrow H_2O + H
\end{array}
$$
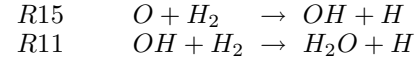
although some important fraction of the atomic oxygen returns to SiO from OH via reaction R10

$$
\begin{array}{lll}
R10 & OH + Si & \rightarrow SiO + H
\end{array}
$$
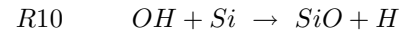
and through CO_2 via reactions R14+R16

$$
\begin{array}{lll}
R14 & OH + CO & \rightarrow CO_2 + H \\
R16 & CO_2 + Si & \rightarrow SiO + CO
\end{array}
$$

It is known in materials science that oxidation of solid SiC through a flow of O_2 at temperatures of ~ 1000 K produces solid SiO_2 and also CO and CO_2 molecules that diffuse trough the lattice and are released to the gas phase (see Wang et al. 2001 and references therein). Therefore, some fraction of the oxygen entering solid SiC grains begin to build the SiO_2 lattice while the rest is released as CO and CO_2. In the region of the CSE where SiC grain formation occurs, the temperatures are similar to those described above but the conditions are somewhat different since it is an oxygen-deficient environment. Nevertheless, if SiO depletes on SiC grains, some fraction of the oxygen can be processed in the grain and released as CO and CO_2. We have run our model assuming that the oxygen of the SiO depleted on SiC grains is released to the gas phase as CO_2 instead of atomic oxygen. Both H_2O and SiO compete for the oxygen contained in the CO_2 molecules through reactions R13 and R16 respectively

$$
\begin{array}{lll}
R13 & CO_2 + H_2 & \rightarrow H_2O + CO \\
R16 & CO_2 + Si & \rightarrow SiO + CO
\end{array}
$$
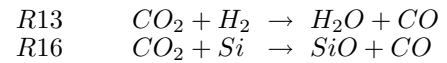
but the high activation energy of R13 prevents water from reaching a high abundance.

(iii) Now we will consider the effect that *shocks* have on oxygen chemistry. In Fig. 4 we plot the evolution of some abundances as the gas moves along the temperature and density profiles given by model MH (see Fig. 2), in order to compare with Willacy & Cherchneff (1998) who used high density values. We also plot the LTE abundances expected for the temperature and density profiles used, so we can see how the abundances predicted by chemical kinetics deviate from the LTE ones. Within the time interval associated to one shock plus relaxation, the immediately post-shocked gas has dissociated a certain fraction of CO releasing atomic oxygen which has a large abundance during the first stages. This atomic oxygen is progressively returned to CO during the relaxation time, but also to OH which has an appreciable abundance during these first stages. Reaction R11
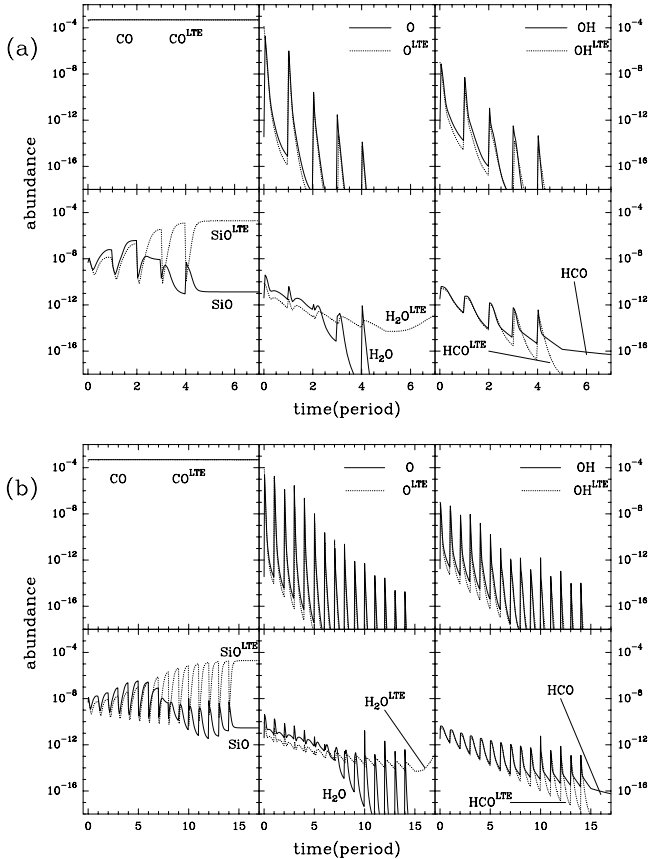
FIG. 4.— Evolution of the abundances, relative to total number of hydrogen nuclei, of some oxygen bearing molecules for a (a) 5 shocks history (N_{shocks}=5) and (b) 15 shocks history (N_{shocks}=15). The history starts at r_0 (t=0) and reaches r_c at time $N_{shocks} \times P$. The LTE abundances for the physical conditions of the gas at each instant are shown as dotted lines.

($OH+H_2 \rightarrow H_2O+H$), which forms water from OH, operates, but at these high temperatures the reverse reaction immediately destroys the H_2O formed, returning oxygen into OH and some time later into CO. Indeed, shocks are a very good mechanism for dissociating CO and releasing atomic oxygen. This $CO \rightarrow O$ process occurs preferably during the first shocks due to the high temperatures, which also make the kinetics of the $O \rightarrow H_2O$ process fast but, since water is not thermodynamically abundant at high temperatures in a C-rich gas (it is at low temperatures), other reactions are faster and return the atomic oxygen to CO.

SiO is very affected by the high non-equilibrium chemistry driven by shocks and ends this phase with a very low abundance, mainly due to reaction R8, which was not included by Willacy & Cherchneff (1998). Note that either considering 5 or 15 shocks to reach r_c from r_0, the abundances do not appreciably change. It is shown that this mechanism decreases rather than enhances oxygen chemistry.

Concerning the H/H_2 ratio, shocks favor a large value since H_2 is dissociated in the post-shocked gas (due to the high temperatures reached) and depending on the density it can regenerate during the relaxation time via the three body reactions R1, R2 and R3 (with high densities, see Fig. 2d) or freeze its abundance at some moment during the relaxation (with low densities, see Figs. 2e and 2f). Again, with a shocks mechanism, a

high density scenario is required to have hydrogen in molecular form.

In summary, O–bearing species are not produced efficiently by gas phase chemistry in the inner envelope, neither considering an expansion at constant velocity nor assuming shocks. Nevertheless, the high water abundance obtained under the LTE assumption suggests that grains may be playing an important role in the recycling of oxygen from CO to H_2O.

4.2. *Oxygen chemistry in the outer envelope*

The chemistry in the outer envelope is mainly driven by the photodissociation of molecules by the interstellar UV field followed by rapid neutral-neutral reactions. This mechanism forms species such as polyynes and cyanopolyynes from photodissociation of parent species such as C_2H_2 and HCN (Millar & Herbst 1994). Concerning oxygen, the photodissociation of CO occurs at the very outer edge of the envelope due to self-shielding (much further away than the photodissociation of C_2H_2 and HCN) so atomic oxygen is abundant only at large radii in the CSE, where the density has decreased considerably and reactions are very slow. This fact makes oxygen chemistry to be much poor than carbon chemistry, since oxygen keeps locked into CO along most of the envelope. The inclusion of the isotopologue ^{13}CO, $\sim$45 times less abundant than parent CO (Cernicharo et al. 2000), which does not self-shield due to its lower abundance, can enhance O abundance at shorter radii. This allows for the formation of some O–bearing species with moderate abundances through rapid neutral–neutral reactions and radiative associations.

Ionic chemistry is triggered by cosmic rays ionization. Cosmic rays can penetrate deeper than UV photons in the CSE since they are not affected by opacity. Ions can react very rapidly via ion-molecule reactions but the chemistry they can induce is limited by the low abundance of ions in the CSE except at the very outer edge (where for example all the carbon is converted into C^+). In our model, ionic chemistry does not noticeably affect the abundances of the O–bearing species formed except for SO, whose abundance is greatly enhanced, and for HCO^+, produced with a low abundance but enough for being detected due its large dipole moment (4.07 D). Another important effect of ionic chemistry is the fractionation of CO through the exchange reaction R26

$$R26 \qquad ^{13}C^+ + ^{12}CO \rightarrow ^{12}C^+ + ^{13}CO$$

which is known to be exothermic by 35 K. Below this temperature the reverse reaction does not operate and ^{12}CO is effectively transformed into ^{13}CO. The net effect is a delay in the destruction of ^{13}CO: its abundance remains nearly constant due to a steady state in which it is formed by the mentioned exchange reaction while it is destroyed by UV photodissociation.

The abundances predicted in the outer envelope for CO, ^{13}CO, O, SiO and HCO^+ (usual O–bearing species in a C-rich star) are shown in the left part of Fig. 5 . The second column of panels show the abundances predicted for H_2O, OH and H_2CO (the three "unexpected" oxygen species), while the rest of panels to the right show the abundances for some other O–bearing species. H_2CS abundance distribution is also shown together with those
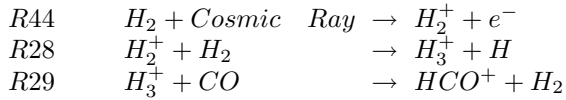
of C_2H and CN, peaking at $\sim$15" and $\sim$20" respectively (see appendix B). We now describe individually the reactions that lead to their abundances, which are expressed relative to total number of hydrogen nuclei rather than relative to H_2:

– **SiO** is formed in the inner envelope and its abundance remains nearly constant throughout the outer envelope until it is dissociated by UV photons (R41). Ionic chemistry destroys SiO at a shorter radius by reacting with C^+ via R27
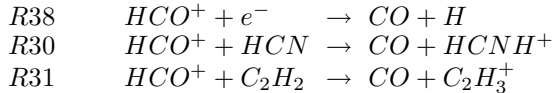
$$R27 \qquad SiO + C^+ \; \rightarrow \; Si^+ + CO$$

However, we point out that SiO could enter the outer envelope with a much lower abundance due to condensation on grain surfaces.

– **HCO$^+$** is produced by the same sequence of reactions that forms it in dark clouds.

$$
\begin{aligned}
R44 &\qquad H_2 + Cosmic \;\; Ray \; \rightarrow \; H_2^+ + e^- \\
R28 &\qquad H_2^+ + H_2 \qquad\qquad \rightarrow \; H_3^+ + H \\
R29 &\qquad H_3^+ + CO \qquad\qquad \rightarrow \; HCO^+ + H_2
\end{aligned}
$$

First, H_2 is ionized by cosmic rays (R44), then H_2^+ reacts with H_2 producing H_3^+ (R28), which in turn reacts rapidly with CO through a proton transfer reaction (R29). The origin of HCO$^+$ is different with respect to the rest of oxygen bearing species commented in this section because its formation does not require the photodissociation of CO but the presence of H_3^+, the formation of which is related to cosmic rays. HCO$^+$ is abundant at shorter radii than the rest of O–bearing species with a peak abundance of 4.5×10^{-10} at 3×10^{16} cm, and a corresponding column density of 1.1×10^{12} cm^{-2}. The abundance profile sharply falls after its peak mainly due to dissociative recombination R38 (electron density becomes important beyond 5×10^{16} cm) and to a less extent, due to proton transfer with HCN and C_2H_2 (reactions R30 and R31 respectively).

$$
\begin{aligned}
R38 &\qquad HCO^+ + e^- \quad \rightarrow \; CO + H \\
R30 &\qquad HCO^+ + HCN \; \rightarrow \; CO + HCNH^+ \\
R31 &\qquad HCO^+ + C_2H_2 \; \rightarrow \; CO + C_2H_3^+
\end{aligned}
$$

– **H$_2$O** formation in C-rich environments, where atomic oxygen is available from the photodissociation of CO, is possible through the route of reaction R15 followed by reaction R11.

$$
\begin{aligned}
R15 &\qquad O + H_2 \quad \rightarrow \; OH + H \\
R11 &\qquad OH + H_2 \; \rightarrow \; H_2O + H
\end{aligned}
$$
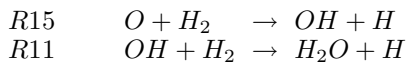
This is the mechanism that forms water in the C-rich protoplanetary nebula CRL618 (see Cernicharo 2004), where temperatures in the inner slowly expanding envelope are $\sim$300 K. However, in the outer envelope of IRC+10216 such high temperatures are not expected and this route does not work, since both reactions R15 and R11 have activation energies that result in negligible rates. In our model, water forms through the radiative association between atomic oxygen and molecular hydrogen (R45).

$$R45 \qquad O + H_2 \; \rightarrow \; H_2O + h\nu$$
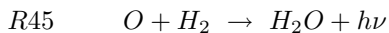
To our knowledge, neither experimental nor theoretical studies have made an estimation of this rate. We have assumed a temperature independent rate constant of 10^{-18} cm^3 s^{-1}, typical of radiative associations between neutral species. Reaction R45 implies breaking

the H_2 bond so that atomic oxygen can insert in, which will result on some activation energy. However, similar reactions, e.g. H_2+C (Le Teuff et al. 2000) and H_2+CH (Brownsword et al. 1997) take values 10^{-17}-10^{-18} cm^3 s^{-1}. Water is produced over an extended region from 4×10^{16} to 6×10^{17} cm with a peak abundance of 10^{-10} and a column density of 4×10^{11} cm^{-2}. These values are far below the abundance estimated from the observations of SWAS (2-12$\times10^{-7}$, Melnick et al. 2001) or ODIN (1.2×10^{-6}, Hasegawa et al. 2006) by at least three orders of magnitude. We will discuss in §4.3 if water originated in this way can or cannot explain the observations.

– **OH** is produced from the photodissociation of water (R42) and from atomic oxygen through both the bimolecular reaction R17

$$R17 \qquad O + NH_2 \; \rightarrow \; OH + NH$$

and the radiative association between O and H (R36). As the gas expands, reaction R36 becomes slower due to the decrease in density although it is compensated by the increase in atomic oxygen abundance. The result is an increase of OH abundance only at the very outer envelope, shown in Fig. 5 as a peak at 6×10^{17} cm. In fact, the O–bearing molecules formed by radiative associations show an extended distribution (reactants such as atoms increase their abundances while expanding) whereas those formed by bimolecular reactions show a peak distribution (reactions only proceed in a shell where reactants are abundant before they are photodissociated). OH could also be produced in reactions of O with several abundant hydrocarbons (e.g. C_nH_2, C_nH, $HC_{2n+1}N$) through H abstraction. However, the reactions of atomic oxygen with closed-shell species such as C_2H_2, C_4H_2 and HCN have activation barriers whereas in reactions with radicals the H abstraction channel seems to proceed slowly. For example, the reaction O+CH→C+OH has been studied by Murrell & Rodriguez (1986) who estimated a negligible reaction rate at low temperatures while the reaction of O with C_2H produces mainly CO and CH. OH is predicted with a very extended distribution from 4×10^{16} to 10^{18} cm with a peak abundance of 7×10^{-10} at the very outer edge and a column density of 2×10^{11} cm^{-2}. Ford et al. (2003) have derived an OH abundance of 4×10^{-8} assuming that all OH is produced from the photodissociation of H_2O, which is formed through comet evaporation in the inner envelope. The spatial distribution they obtain ranges from 3×10^{16} cm to 7×10^{16} cm. If OH follows the more extended radial distribution calculated by us, then the beam filling factors and physical conditions of the emitting gas are very different from those assumed by Ford et al. (2003) and we could expect a considerable decrease of the OH estimated abundance.

– **H$_2$CO** is produced through reaction R18

$$R18 \qquad O + CH_3 \; \rightarrow \; H_2CO + H$$
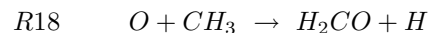
the source of CH_3 being the photodissociation of CH_4 (R43) while atomic oxygen is provided by CO and ^{13}CO photodissociation. The rate for R18 is well known for a temperature range of 259-2500 K in which it does not show a temperature dependence, suggesting a similar value at low temperatures. The peak abundance is 1.4×10^{-9}, reached at 4×10^{16} cm. The abundance derived by Ford et al. (2004) from millimeter observations
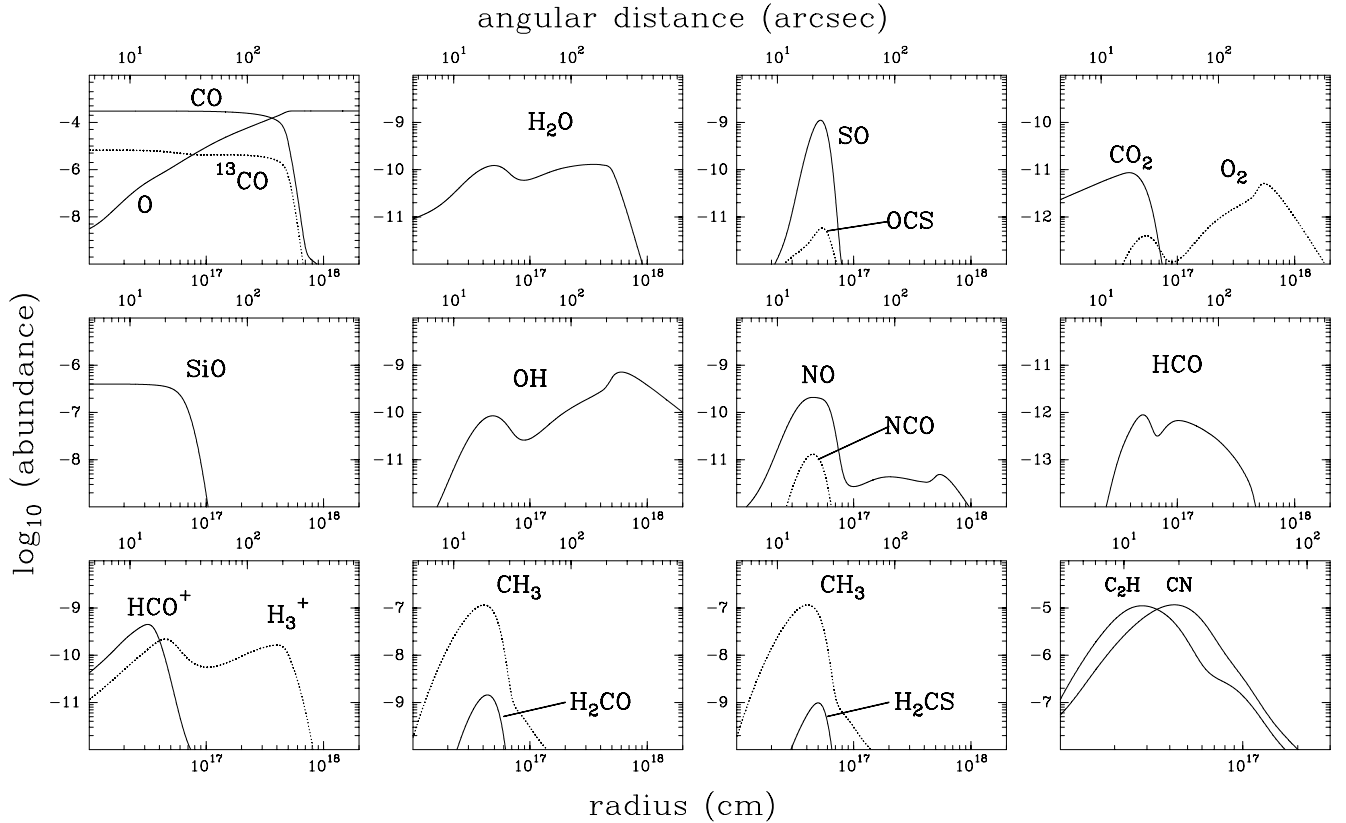
FIG. 5.— Abundances, relative to total number of hydrogen nuclei, for some oxygen bearing molecules in the outer expanding envelope as given by chemical kinetics. C_2H and CN abundances are shown in the bottom-right panel peaking at ∼15" and ∼20" respectively (see appendix B). Angular distance is given in the top axis for an assumed distance to IRC+10216 of 150 pc.

of pure rotational transitions is a factor 5 higher than the one we get with the model. We discuss in §4.3 the compatibility of the abundance predicted by our model with the lines observed.

– **SO** can be formed from OH+S (R19) and from O+SH (R20).

$$R19 \qquad OH + S \; \rightarrow \; SO + H$$
$$R20 \qquad O + SH \; \rightarrow \; SO + H$$
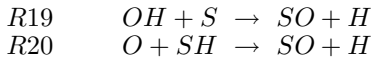
For R19 we take the rate constant measured at 298 K. The rate of reaction R20 has been measured at 298 K and at high temperatures (1100-2000 K) and does not show temperature dependence, so that we assume the same value at low temperatures. In our model the abundance of OH is low in most of the CSE. On the other hand, SH abundance is relatively high due to a sequence of ion-molecule reactions that begin with the charge transfer of C^+ to SiS (R32). The SiS^+ formed this way reacts with H via reaction R33 and produces SH.

$$R32 \qquad SiS + C^+ \; \rightarrow \; SiS^+ + C$$
$$R33 \qquad SiS^+ + H \; \rightarrow \; SH + Si^+$$
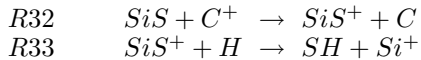
The peak abundance predicted for SO is 1.1×10^{-9} with a column density of 4.7×10^{11} cm^{-2}. However, we point out that SO abundance is greatly influenced by H abundance, for which we have taken an upper limit given by Bowers & Knapp (1987). A process of H_2 formation on grains surfaces, not considered in this model, could reduce the abundance of atomic H, thus decreasing the amount of SO in the outer envelope.

– **OCS** forms by radiative association of S and CO (R37). The predicted peak abundance is 6×10^{-12} with a quite low column density of 7.4×10^9 cm^{-2}.

– **NO** is formed by the bimolecular reaction R21 involving atomic oxygen and NH, which in turn comes from photodissociation of NH$_3$.

$$R21 \qquad O + NH \; \rightarrow \; NO + H$$

The rate for this reaction is a temperature independent estimation for the 250-3000 K range and is assumed to apply also at low temperatures. The predicted abundance is 2×10^{-10} with a column density of 2×10^{11} cm^{-2}, although its low dipole moment (0.159 D) makes difficult its detection.

– **NCO** forms by reaction R22 the rate of which is based on an experimental measurement at low pressure and 292 K and the assumption that formation of NCO is the main channel.

$$R22 \qquad CN + OH \; \rightarrow \; NCO + H$$
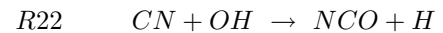
Its predicted abundance is 10^{-11}. The relatively low dipole moment (0.6 D), the large partition function and the low predicted abundance will make very difficult its detection.

– **H$_2$CS** abundance is also shown in Fig. 5. Although it is not an O–bearing species, it is formed through the sulfur analogous reaction that forms H_2CO (R23).

$$R23 \qquad S + CH_3 \; \rightarrow \; H_2CS + H$$
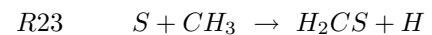
The rate of this reaction has not been measured and therefore it is assumed equal to the oxygen analogous case. Atomic sulfur is necessary, instead of oxygen, and it is provided by the photodissociation of SiS and CS. Ionic chemistry slightly enhances H_2CS abundance since

atomic S is released at short radii through ion-molecule reactions such as R34

$$R34 \qquad SiS + S^+ \; \rightarrow \; SiS^+ + S$$
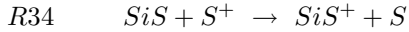
and because more chemical routes for thioformaldehyde formation appear, e.g. from H_3CS^+ through dissociative recombination (R39).

$$R39 \qquad H_3CS^+ + e^- \; \rightarrow \; H_2CS + H$$
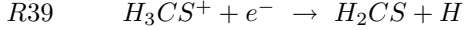
The peak abundance is 10^{-9} with a distribution similar to that of formaldehyde. The predicted abundance profile produces line shapes in reasonable agreement with observations (see below).

– **CO_2** is formed through reaction R35, which involves SiO^+ that is formed with an abundance of $\sim10^{-11}$ from several ion-molecule reactions.

$$R35 \qquad SiO^+ + CO \; \rightarrow \; CO_2 + Si^+$$
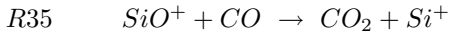
We point out that CO_2 could be also a product of evaporation of cometary ices and will have a large abundance in the cometary scenario. However, an ISO spectrum of IRC+10216 in the mid-infrared with a very large signal-to-noise ratio (Cernicharo et al. 1999) only shows C_2H_2 and HCN lines in the 13-16 μm range and no evidence for CO_2.

– **O_2** formation is strongly related to the presence of OH from which is formed through reaction R24.

$$R24 \qquad O + OH \; \rightarrow \; O_2 + H$$
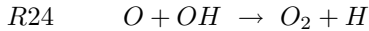
Its spatial distribution follows that of OH with an abundance 2 orders of magnitude smaller.

– **HCO** is produced with a quite low abundance ($\sim10^{-12}$) mainly from atomic oxygen by reaction R25.

$$R25 \qquad O + CH_2 \; \rightarrow \; HCO + H$$

Dissociative recombination of H_2CO^+ (R40) also contributes to HCO formation.

4.3. Comparison with observations

In order to compare with available observations we have performed Monte Carlo radiative transfer calculations for H_2CO, H_2O, HCO^+, SO and H_2CS with the code described in González-Alfonso & Cernicharo (1993). The CSE has been simulated by a spherically distributed expanding gas with the radial profiles for density, temperature and abundance of each species taken from the chemical model. Line profiles and intensities for several transitions are then generated after convolution of the radiative transfer results with the main beam of the selected telescope.

– **H_2CO**. Ford et al. (2004) have observed four pure rotational lines of ortho-H_2CO: $2_{1,2}-1_{1,1}$ (140.840 GHz), $2_{1,1}-1_{1,0}$ (150.498 GHz), $3_{1,3}-2_{1,2}$ (211.211 GHz) and $3_{1,2}-2_{1,1}$ (225.698 GHz) with antenna temperatures of ~30 mK, ~20 mK, ~20 mK and ~20 mK respectively; one line of para-H_2CO: $3_{0,3}-2_{0,2}$ (218.222 GHz) with $T_A^*\sim20$ mK; and failed to detect the low excitation transition of para-H_2CO $1_{0,1}-0_{0,0}$ (72.838 GHz) at a sensitivity of ~10 mK. They also conducted 17" offset observations for the $2_{1,1}-1_{1,0}$ line with an average line intensity reduced by a factor 3-4, which nevertheless indicates an extended H_2CO distribution. We have used the abundance profile obtained from our chemical model to predict the expected line intensities in order to see if the formaldehyde formed through these chemical routes can account for the observed lines. The collisional coefficients, needed for solving the statistical equilibrium, are taken from Green (1991) (corrected for H_2 as collider instead of He) and the normal ortho-to-para ratio of 3:1 has been assumed.

The resulting lines are less intense than the observed ones by a factor 4-10 depending on the line. Nevertheless, one has to keep in mind that the abundances resulting from such a simple chemical model are affected by uncertainties due to missing reactions, uncertain rates and also errors in physical parameters (kinetic temperature, mass loss rate, etc). Formaldehyde is formed from O and CH_3 by reaction R18

$$R18 \qquad O + CH_3 \; \rightarrow \; H_2CO + H$$
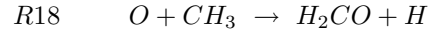
so the abundances of the two reactants together with the rate of R18 directly affect the abundance that H_2CO may reach. The rate constant for reaction R18 is known down to 259 K, but not for the much lower temperatures that are present in the outer envelope of IRC+10216. We could expect a higher rate constant at very low temperatures, a behavior experimentally observed in many other radical-molecule reactions without activation energy (see Smith et al. 2004 and references therein). Another important parameter is the branching ratio for CH_3 production in methane photodissociation by the interstellar UV field, for which Le Teuff et al. (2000) give a 15%. For the solar UV field values up to 44% are commonly used (see the chemical model of Saturn's atmosphere by Moses et al. 2000). Although the energy distribution of the interstellar and solar UV field are somewhat different, we could expect larger uncertainties in the former one. When we increase R18 rate constant by a factor of 3 and the CH_3 branching ratio by a factor of 2, the resulting H_2CO abundance (see solid line in right-down panel of Fig. 6) increases by a factor of ~6 with respect to the former model (that of Fig. 5). A comparison of the spectral lines resulting from such abundance profile with the lines observed by Ford et al. (2004) give us several conclusions: (1) the line intensities agree quite well for the ortho-H_2CO lines whereas for the para-H_2CO the agreement is worse: the 72.838 GHz line is predicted a factor ~3 more intense than the observed upper limit and the 218.222 GHz line is predicted a factor 2-3 less intense than the observation. Uncertainties in the collisional coefficients, ortho-to-para ratio or in the temperature and density profiles used could explain the discrepancies between model and observations. (2) The ratio of the integrated intensity between the 17" offset position to the centered one in the 150.498 GHz line is 0.87, in contrast with the value of 0.4 obtained from the observations. Sources for the disagreement can be errors in the pointing, the uncertainty in the distance to the star or the depart from spherical symmetry in H_2CO emission. (3) One last aspect to point out is the different shapes of the observed and predicted 1.3 mm lines of ortho-H_2CO (at 211.211 and 225.698 GHz). The predicted lines have pronounced double-peaked shapes with almost no emission at zero velocity, as corresponds to a shell with a certain size (diameter of ~40" in the model) observed with a smaller telescope beam (~11" for IRAM-30m at those frequencies). On the other hand the observed lines
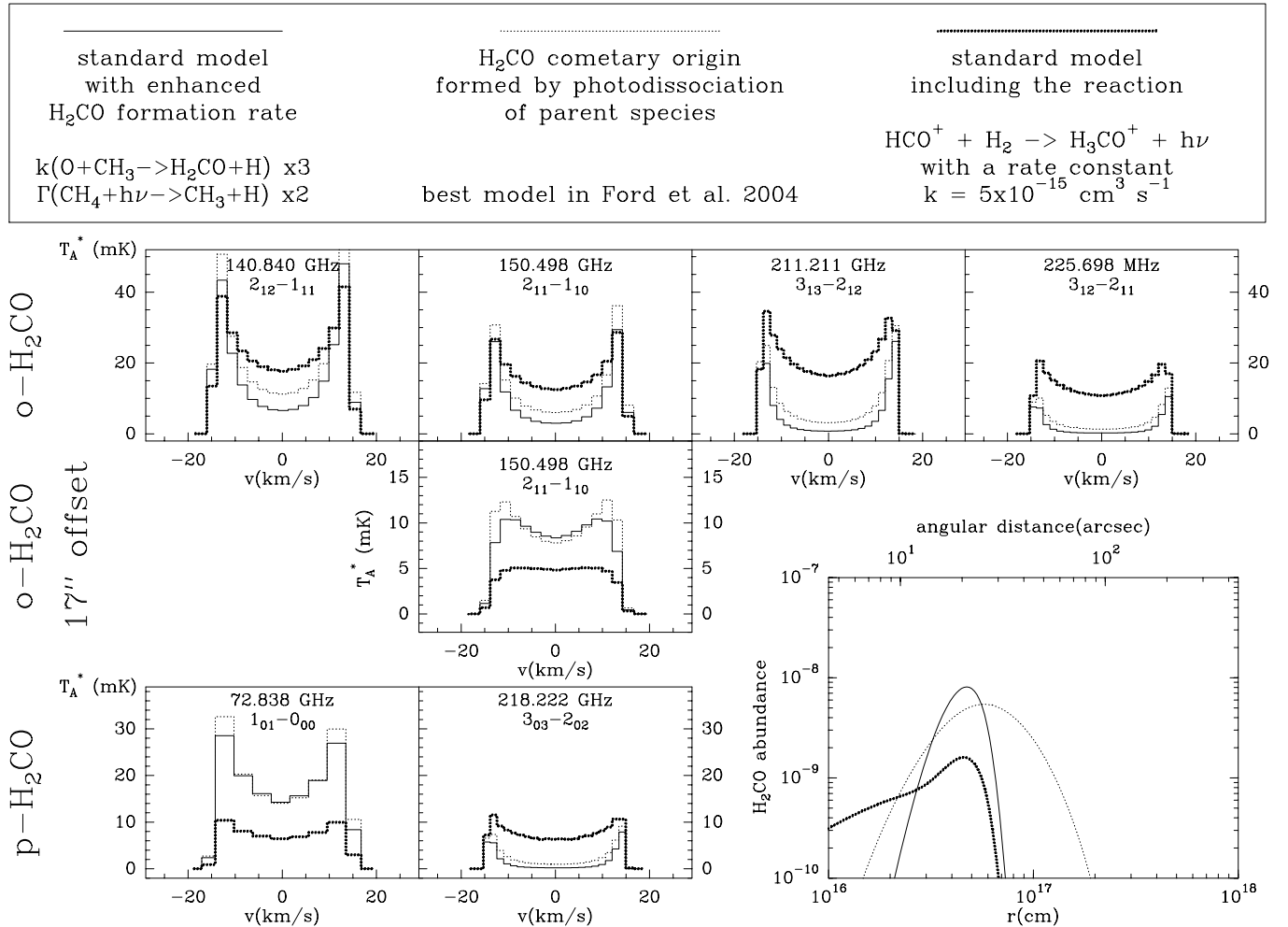
FIG. 6.— Calculated line intensities and profiles for pure rotational transitions of ortho-H_2CO and para-H_2CO. The lines should be compared with the observations reported by Ford et al. (2004). IRAM-30m beam size has been considered and the lines have been smoothed to a resolution of 1 MHz. The H_2CO abundances, relative to total number of H nuclei, are plotted in the bottom-right panel. –Solid lines: H_2CO abundance resulting from the chemical model with two parameters slightly changed: R18 rate constant increased in a factor 3 and the CH_3 branching ratio in methane photodissociation increased from 15% to 30%. –Faint dotted lines: H_2CO produced from photodissociation of an unknown parent species, which would be released by sublimation of the mantles of comets, assumed to be present in the inner envelope. Best model in Ford et al. (2004). –Hard dotted lines: H_2CO abundance resulting from the chemical model including reaction R46 in order to increase formaldehyde abundance in the inner regions.

show substantial emission at zero velocity and a less pronounced double-peaked profile. Neither an error of up to 4" in the pointing observations nor a larger distance to the star of up to 200 pc (more will make IRC+10216 to be overluminous for its type according to Crosas & Menten 1997) will appreciably change the predicted line profiles.

Ford et al. (2004) interpret the presence of formaldehyde as a direct product from the photodissociation of an unknown parent molecule released in the inner envelope by cometary sublimation. Such interpretation is supported by the observation of extended emission of formaldehyde toward the comet P/Halley (Meier et al. 1993). Ford et al. (2004) constructed a simple model with the following parameters: initial abundance of the parent species relative to H_2 of 8×10^{-8}, unattenuated photodissociation rate of the parent species producing H_2CO of $A_p=1.6\times10^{-10}$ s^{-1} and unattenuated photodissocation rate of formaldehyde $A_{H_2CO}=7.81\times10^{-10}$ s^{-1}, which reproduced the observed line intensity of the 150.498 GHz line and the ratio $(\int T_A^* dv_{off})/(\int T_A^* dv_{cent})$ of 0.4 for this line. We have run a model with the same parameters to obtain the abundance distribution and the

expected line profiles (light dotted lines in Fig. 6). It is seen that the abundance distribution is more extended than the previous one although the 1.3 mm line profiles of ortho-H_2CO still show an emission at zero velocity too low compared with the observations. The abundance distribution of H_2CO with a cometary origin is somewhat similar to the one we get with the chemical model, because in both cases formaldehyde is produced in the region where interstellar UV photons penetrate.

From the above considerations it follows that an increase of the formaldehyde abundance in the inner regions of the CSE is needed for producing some emission at zero velocity and matching the observations. Formation of H_2CO in inner regions can be explained by hydrogenation of CO on grain surfaces followed by photodesorption (species such as CH_4, NH_3 and H_2S are thought to be formed by similar processes). Since this possibility is very complex to model, we have investigated if some missing gas phase reactions can enhance formaldehyde abundance at short radii. At this point it is worth to note that HCO^+ has an abundance distribution peaking closer to the star than the one of H_2CO (see Fig 5) and that

produces double-peaked spectral lines but with substantial emission at zero velocity (see Fig. 8). As discussed for HCO$^+$ formation, ionic chemistry is initiated by cosmic rays at shorter distances than photochemistry does since the CSE is not opaque to cosmic rays. Formaldehyde can also be formed from H$_2$CO$^+$ (through charge transfer with several species) and H$_3$CO$^+$ (through dissociative recombination) but in our model these routes are not important since both H$_2$CO$^+$ and H$_3$CO$^+$ are not abundant enough. Looking at exothermicity we can examine possible missing reactions that can contribute to the formation of these two species (heats of formation have been taken from NIST Chemistry Webbook[2] and Le Teuff et al. 2000). One possibility is the reaction H$_3^+$+CO for which the only exothermic channels are the well known proton transfer giving HCO$^+$ and the radiative association which produces H$_3$CO$^+$. Another possibility is the reaction HCO$^+$+H$_2$ but all the investigated channels are highly endothermic due to the high stability of both reactants and only the radiative association producing H$_3$CO$^+$ is exothermic by 123 kJ/mol. We find that including the reaction HCO$^+$+H$_2$ $\rightarrow$ H$_3$CO$^+$+hν with a rate constant of 5×10^{-15} cm^3 s^{-1} (R46), the formaldehyde abundance is enhanced at the inner regions producing rotational lines in agreement with the observations, i.e. with significant emission at zero velocity (strong dotted lines in Fig. 6). All the lines except the one at 218.222 GHz of para-H$_2$CO (predicted a factor 2 less intense than observed) agree very well with the observations in intensity and profile. The required rate constant is typical of other ion-neutral radiative associations (Le Teuff et al. 2000).

Finally, is it worth to note that three of the four unidentified lines in Ford et al. (2004) can be assigned as follows: U150 is the $7_{1,7}$-$6_{1,6}$ transition of Si^{13}CC at 150385.281 MHz (Cernicharo et al. 1991, 2000); U218b is the N=23-22 J=45/2-43/2 transition of CC^{13}CCH at 218103.281 MHz (Cernicharo et al. 2000); and U218a is one component of the $^2\Pi_{1/2}$ J=45/2-43/2 transition in the ν_7=1 vibrational state of C$_4$H at 218287.460 MHz (Guélin et al. 1987b; Yamamoto et al. 1987; Cernicharo et al. 2000).

– **H$_2$O**. The evidence for water presence in IRC+10216 comes from the detection of the ortho transition $1_{1,0}$-$1_{0,1}$ at 556.936 GHz with the telescopes SWAS (T_A^*~20 mK, Melnick et al. 2001) and ODIN (T_{MB}~50 mK, Hasegawa et al. 2006). In order to model the radiative transfer of water throughout the CSE we consider the lowest lying 8 rotational levels in the vibrational ground state level (ν_1,ν_2,ν_3)=(0,0,0), in the first excited bending mode (0,1,0) and in the first excited asymmetric stretching mode (0,0,1). The ortho-H$_2$O–He collisional rates from Green (1993), corrected for H$_2$ as collider, are adopted for all the transitions within the same vibrational level, whereas for ro-vibrational transitions collisions are not considered important.

Excitation to the ν_2=1 state occurs by absorption of λ~6 μm photons whereas excitation to the ν_3=1 state corresponds to λ~3 μm. Photons at these two wavelengths are abundant within the CSE due to the presence of the central star and dust, so these excited vibrational levels can be easily populated. Furthermore, since our chemical model predicts water to be abundant in the outer CSE, where densities range from 10^5 to 10^2 cm^{-3} (n$_{crit}$~10^9 cm^{-3} for the 556.936 GHz transition), collisional excitation is not effective to populate the $1_{1,0}$ state and the dominant excitation mechanism is radiative pumping to the ν_2=1 and ν_3=1 vibrational excited states followed by radiative decay to several rotational levels of the vibrational ground state, included the $1_{1,0}$ state.

In our chemical model water is formed through the radiative association R45

$$R45 \qquad O + H_2 \;\rightarrow\; H_2O + h\nu$$
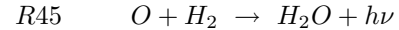
with an assumed rate constant of 10^{-18} cm^3 s^{-1}. As noted in §4.2, the abundance reached with such a rate constant is not enough to explain the observed 556.936 GHz line. Since the rate constant for this reaction is not known and water abundance approximately scales with this rate, we have fitted R45 rate to get a 556.936 GHz line intensity in agreement with the observations. We find that it is necessary to increase the rate constant up to ~10^{-15} cm^3 s^{-1}. The peak abundance obtained then is ~10^{-7} as shown in Fig. 7 . With such an abundance profile, we have performed Monte Carlo radiative transfer calculations. We show in Fig. 7 the lines predicted for ODIN in different scenarios in which the fluxes at λ=3 and 6 μm vary. On the left side the central star has been considered as a blackbody at T=T_* with and without dust throughout the CSE. We consider carbonaceous grains with sizes between 0.01 and 1 μm and a gas-to-dust mass ratio of 500 (Knapp 1985). It is seen that the presence of dust enhances the 557 GHZ line intensity since grains absorb the photons from the star (its maximum is at λ=2 μm) and reemits at longer wavelengths, thus enhancing the flux at λ=6μm and exciting the bending mode of H$_2$O. In fact, the IR spectrum of IRC+10216 as observed by ISO (Cernicharo et al. 1999) peaks at 10 μm due to the presence of dust and approximately corresponds to a blackbody of radius 20 R$_*$ with a temperature of ~500 K. We can therefore simulate the IR flux that water in the outer envelope would receive by putting such a blackbody instead of the star. In Fig. 7 we see how the 556.936 GHz line intensity increases when the flux at λ 6 μm is enhanced by considering a blackbody with increasing temperature. These radiative transfer models show the importance of the IR pumping of the excited vibrational levels of H$_2$O for the intensities of pure rotational lines in the ground vibrational state.

In summary, assuming a rate constant of 10^{-15} or a few 10^{-16} cm^3 s^{-1} for R45 we can reproduce the water line observed by ODIN. Now the question is how reasonable is such a high rate constant for a radiative association between neutrals. This reaction is spin-forbidden according to Wigner-Witmer rules since the potential energy surfaces (PES) of reactants and products in their ground electronic states, H$_2$($^1\Sigma$)+O(^{3}P)$\rightarrow$H$_2$O(^{1}A)+hν, are not connected adiabatically. For the reaction to proceed, an intersystem crossing between PES with different total electronic spin has to occur during the reaction. A spin-forbidden reaction is likely to have a small rate constant, however some other reactions in which reactants and products do not adiabatically correlate have been

---

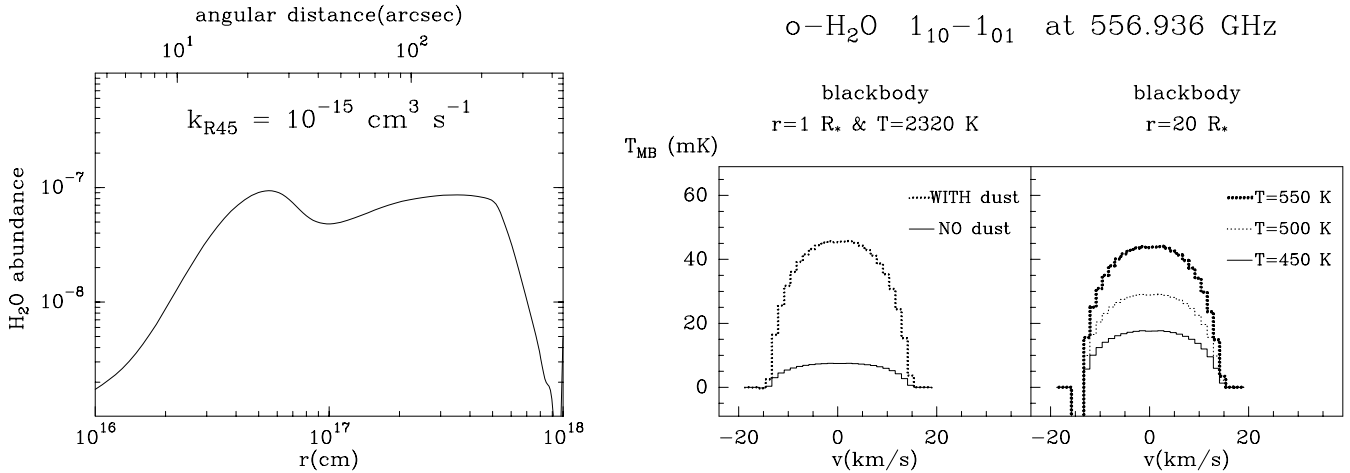[2] The NIST Chemistry Webbook is available on the World Wide Web at http://webbook.nist.gov/chemistry/.

FIG. 7.— –Left: Water vapor abundance, relative to total number of H nuclei, when assuming a rate constant for R45 of 10^{-15} cm^3 s^{-1}. –Right: calculated line intensities and profiles for the $1_{1,0}$-$1_{0,1}$ transition of ortho-H$_2$O for different IR fluxes. ODIN beam size ($\sim 2'$) has been considered and the lines have been smoothed to a resolution of 1.3 km/s.

found to be very rapid. For example the bimolecular reaction: C(^{3}P)+C$_2$H$_2$($^1\Sigma$)→C$_3$($^1\Sigma$)+H$_2$($^1\Sigma$) may have a rate constant of several 10^{-10} cm^3 s^{-1} at very low temperatures (Clary et al. 2002) while the radiative association HS$^+$($^3\Sigma$)+H$_2$($^1\Sigma$)→H$_3$S$^+$(^{1}A)+hν has a rate constant of 7×10^{-16} cm^3 s^{-1} at 80 K (Herbst et al. 1989).

A high rate constant for reaction R45 would also have consequences for the chemistry in dark clouds. If k$_{R45}$=10^{-15} cm^3 s^{-1}, and with a typical density of 10^4 cm^{-3}, the chemical time scale to produce water from atomic oxygen would be as short as 3×10^3 years. Chemical models without this radiative association predict H$_2$O abundances somewhat higher than the observational upper limits imposed by SWAS (Roberts & Herbst 2002). Nevertheless, depletion on grains at late times would reduce the water vapor abundance so that models could match the observations. In diffuse clouds, with lower visual extinctions ($A_v\sim1$) and densities ($n_H\sim100$ cm^{-3}), reaction R45 would also produce water in time scales of 3×10^5 years, with an abundance relative to H$_2$ of $\sim3\times10^{-7}$ in steady state[3]. This value is 1–2 orders of magnitude higher than the scarce observational estimations available (Spaans et al. 1998; Neufeld et al. 2002). Nevertheless, in diffuse clouds a significant fraction of hydrogen is not in molecular form, therefore the rate of water formation through reaction R45 would be lower than our estimation. Furthermore, since the observations of interstellar water ice bands do not discriminate between different types of clouds, dense or diffuse, present along the line of sight (e.g. Schutte et al. 1998; Moneti et al. 2001), it is highly uncertain whether the amount of water as solid ice is important or not.

There are other clues, apart from the 557 GHz line, that will help in understanding the water origin in this late-type C-rich star: (1) If water is formed in the outer envelope it will have a spherical shell-like distribution

while Fischer-Tropsch and cometary hypotheses will produce a solid sphere-like distribution since both require water to be formed much closer to the star. Herschel Space Observatory will be able to distinguish between these two possibilities since its beam size will be much narrower than those of SWAS and ODIN. (2) The absence of pure rotational and ro-vibrational lines of water in the ISO far-IR spectrum analyzed by Cernicharo et al. (1996) discards the presence of a significant amount of water in the inner envelope. (3) As noted by Rodgers & Charnley (2002), the cometary origin implies the presence of HDO with an abundance ~0.06 % relative to H$_2$O. HDO detection would demonstrate that water is not formed from material ejected by the star and the cometary hypothesis would be the only one reasonable.

– **HCO$^+$**. Its presence in IRC+10216 has been debated for years. Chemical models (Glassgold et al. 1986) predicted it with an abundance high enough to allow its detection with available millimeter or submillimeter telescopes. On the other hand, observations did not clearly probe its existence. The J=1-0 line (with an intensity of T_A^*=20 mK with the IRAM 30m telescope, see Fig. 8) often has been observed as a weak feature at the noise level (Lucas & Guélin 1990). The J=4-3 line was observed as a weak feature of $T_A^*\sim25$ mK with the JCMT telescope by Avery et al. (1994). However, they failed to detect the J=3-2 line at a noise level of ~10 mK, which was predicted with $T_A^*\sim45$ mK on the basis of a rotational temperature of 17 K obtained from the intensities of the J=1-0 and J=4-3 lines. These considerations led these authors to conclude that the feature at the J=4-3 frequency was not arising from HCO$^+$ and they calculated an upper limit for its column density of 1.4×10^{11} cm^{-2}. Our Monte Carlo radiative transfer calculations show that the excitation temperatures of each line are significantly different, thus a prediction of the expected intensities of other lines with a unique T_{rot} should be taken with care. To calculate the line profiles of HCO$^+$ we have decreased by a factor of 2 the abundance profile obtained with the chemical model in order to match the observed J=1-0 line. HCO$^+$ is formed through the sequence of reactions R44+R28+R29 and therefore its
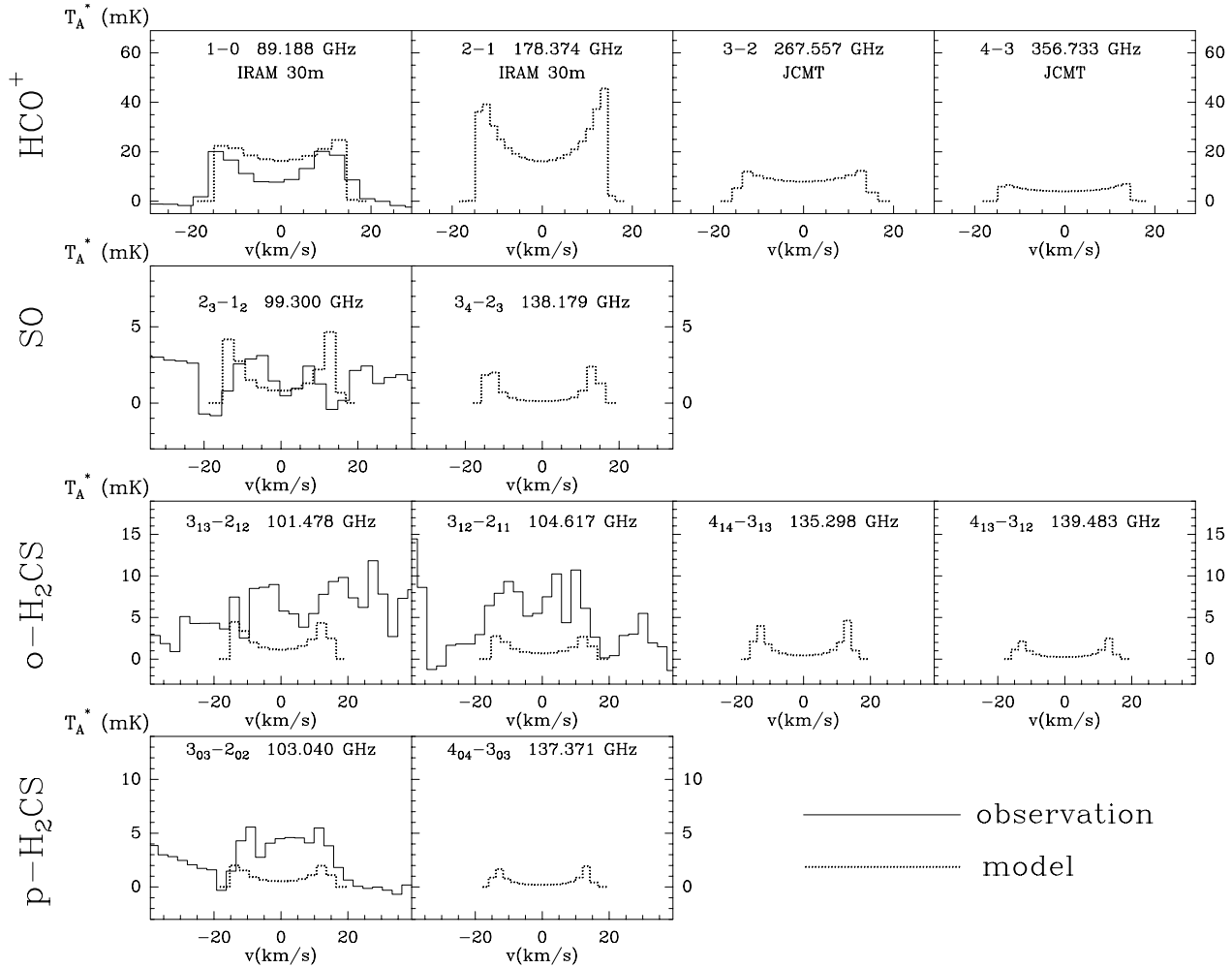
---

[3] The H$_2$O abundance reaches the steady state when the formation and destruction rates become equal. If we assume that reactions R45 and R42 are the main formation and destruction routes, then n(H$_2$O)/n(H$_2$) = [k_{R45} x_O n_{H_2}]/[G_0 5.9×10^{-10} exp(−7.1 A_v)], where x_O is the O abundance relative to H$_2$ and G_0 is the UV field relative to the interstellar standard one (see appendix B). If we take A_v=1, G_0=1, x_O=6$\times10^{-4}$, k_{R45}=10^{-15} cm^3 s^{-1} and n(H$_2$)=n_H/2=100/2 cm^{-3} (assuming hydrogen is mainly molecular), we get n(H$_2$O)/n(H$_2$) = 3×10^{-7}.

FIG. 8.— Calculated line intensities and profiles for pure rotational transitions of HCO$^+$, SO, ortho-H$_2$CS and para-H$_2$CS. All lines have been smoothed to a resolution of 1 MHz except the 3-2 and 4-3 of HCO$^+$ which have been smoothed to a 2 MHz resolution. All lines are calculated for IRAM 30m telescope except the 3-2 and 4-3 which have been calculated for the JCMT telescope. The abundance profiles used are given by the chemical model (those of Fig. 5) except that of HCO$^+$, which has been decreased by a factor 2 for matching the J=1-0 line observed. The model is plotted as dotted lines and the λ 3 mm observations from Cernicharo et al. (2006) as solid lines.

abundance depends basically on the rates of these reactions as well as on the destruction rates. The most uncertain of all of them is the ionization by cosmic rays of H$_2$ (R44), which depends on the cosmic rays field in the surroundings of IRC+10216. The abundance of HCO$^+$ approximately scales with R44 rate. Therefore, a decrease by a factor of 2 in the cosmic rays field would explain the decrease in abundance needed to match the J=1-0 observed line.

The predictions for the first four pure rotational transitions are shown in Fig. 8. It is seen that the excitation conditions are such that the J=3-2 line is expected with a slightly higher intensity than the J=4-3 line, both being ∼10 mK in T_A^* for the JCMT telescope. This suggests that the 25 mK feature observed by Avery et al. (1994) at the frequency of J=4-3 is indeed not arising from HCO$^+$ because the J=3-2 was not detected above a 10 mK noise level. Future long time-integrated observations of these two lines will definitively establish the excitations conditions of HCO$^+$ in IRC+10216.

– **SO**. The abundance reached by SO in the chemical model is enough to produce some lines with intensities

of a few mK. Fig. 8 shows the N_J=2$_3$-1$_2$ and 3$_4$-2$_3$ expected line intensities together with a feature at 99.300 GHz of a spectrum, obtained with the IRAM 30m telescope (Cernicharo et al. 2006), which could correspond to the 2$_3$-1$_2$ transition. A higher signal-to-noise ratio for this spectrum is needed to claim detection. Long time-integrated observations at the frequencies of other SO transitions (e.g. the 3$_4$-2$_3$) would decide about the existence of SO in IRC+10216 formed trough the ion-molecule chemical sequence of R32+R33 followed by the neutral-neutral reaction R20.

– **H$_2$CS**. The chemical model predicts that this molecule is produced with a moderate abundance, both through neutral chemistry (from S+CH$_3$, R23) and through ionic chemistry (from H$_3$CS$^+$, R39). The abundance reached is within the same order of magnitude than for H$_2$CO, but less intense rotational lines are expected due to its smaller dipole moment (1.649 D versus 2.331 D of formaldehyde). We have also assumed an ortho-to-para ratio of 3:1. Fig. 8 shows the expected line profiles of ortho and para H$_2$CS, together with some features from a λ 3 mm spectrum taken with the IRAM 30m telescope (Cernicharo et al. 2006). The features have intensities

somewhat higher than the predicted ones, but with the right order of magnitude.

5. CONCLUSIONS

LTE chemical models predict that O–bearing species such as water are very abundant in the inner envelope of IRC+10216. However, a more realistic non-LTE approach, based on chemical kinetics, indicates that the transformation of CO into H_2O within the gas phase is not efficient in the inner layers, because of the high energies required to break the CO bond. On the other hand, the increase of SiO abundance with radius, predicted in LTE, is possible because the reaction Si+CO→SiO+C is competitive in a high density scenario for the inner envelope. An alternative mechanism for water production out of the gas phase could be related to grain surfaces, which can act as a catalyst reducing the activation energy for either a CO→H_2O process (due to Fischer-Tropsch catalysis according to Willacy 2004) or a SiO→H_2O process (on SiC grains).

Concerning oxygen chemistry in the outer envelope, the release of atomic oxygen due to CO photodissociation allows for the formation of some O–bearing species. The abundance predicted for H_2CO is a factor ∼5 lower than the observational estimation of Ford et al. (2004). Wether formaldehyde is formed by the reaction O+CH_3→H_2CO+H or it is produced from photodissociation of an unknown parent species released from comets, as suggested by Ford et al. (2004), the expected shape of the λ 1.3 mm rotational lines disagrees with the observations. An alternative source of H_2CO is suggested to be the radiative association HCO^++H_2→H_3CO^++hν. The possibility of forming water in the outer envelope depends on the rate constant of the radiative association between atomic oxygen and molecular hydrogen. Nonlocal radiative transfer models show that a rate constant as high as 10^{-15} cm^3 s^{-1} is needed to reproduce the 556.936 GHz line profile observed by SWAS and ODIN telescopes. Quantum chemical calculations of the rate constants of the two radiative associations suggested in this paper, specially the H_2+O reaction, could support or discard them as important reactions in astrochemistry.

Other oxygen bearing species such as SO could exist with abundances and excitation conditions which would produce rotational lines near the detection limit of IRAM-30m telescope. HCO^+ is observed with an intensity roughly in agreement with that predicted from chemical and radiative transfer models. Thioformaldehyde formation is also predicted through a chemical route analogous to that of formaldehyde. This is supported by the agreement of the line profiles obtained from radiative transfer models with observations at λ 3 mm.

Although the evaporation of cometary ices could be the source of water in this late–stage carbon star, other phenomena such as catalysis on grains or the production in the outer envelope through the radiative association of H_2+O could also explain the formation of this O–bearing species in the expanding carbon-rich envelope. Future observations with the Herschel Space Observatory will permit to distinguish the most plausible chemical processes leading to the formation of water vapor in a carbon-rich environment.

APPENDIX

NUCLEATION AND GROWTH OF SIC GRAINS

Here we describe the formation of SiC grains in the inner envelope of IRC+10216 as a two-step process: (1) formation of condensation nuclei plus (2) growth of grains from these nuclei by accretion of gas phase species.

(1) The mathematical description of the nucleation process is mainly taken from Gail et al. (1984). We assume that the expanding gas has at all moments a population of clusters $(SiC)_N$, composed of different number N of SiC monomers, which in thermal equilibrium is given by

$$n_{(SiC)_N} = n_{SiC} \times exp\big(-\Delta G(N)/kT_{gr}\big) \tag{A1}$$

where n means numerical density, T_{gr} is the grain temperature and $\Delta G(N)$ is the free energy of formation of a cluster of size N from the monomers. The temperature of SiC grains T_{gr} is not equal to the kinetic temperature of the gas T_k because the former is affected by an inverse greenhouse effect which makes T_{gr} to be less than T_k (McCabe 1982). To calculate T_{gr} we follow the treatment of this author. The magnitude $\Delta G(N)$ can be expressed as

$$\Delta G(N) = k\theta_N(T_{gr})(N-1)^{2/3} - kT_{gr}(N-1)lnS \tag{A2}$$

where S is the supersaturation ratio (ratio of the SiC vapor pressure to its saturation pressure) that is calculated following McCabe (1982), and the magnitude $\theta_N(T_{gr})$ (described in Draine 1979) is related to the surface tension of solid SiC for large N while for low N is treated as a free parameter since it is unknown.

Once we have establish a population of clusters $(SiC)_N$ given by thermal equilibrium, nucleation theory says that there exist one critical size N_*. Cluster with sizes $N \geq N_*$ will continue accreting growth species (here SiC molecules) resulting in grains of growing size, while clusters with sizes $N < N_*$ will revert to the monomers. Thus, there exists a bottleneck at N_* in the size spectrum. The critical size N_* is found by maximization of $\Delta G(N)$ with respect to N.

The steady state rate J_*^S for the transformation '$(SiC)_{N_*}\rightarrow$nucleus' is given by

$$J_*^S = \underbrace{\left\{ \sum_{i=1}^{N_0} n_i \left(\frac{kT_k}{2\pi m_i}\right)^{1/2} \alpha_i \right\}}_{\beta} \times \underbrace{4\pi a_0^2 N_*^{2/3}}_{A_{N_*}} \times n_{(SiC)_{N_*}} \times Z \tag{A3}$$

The subscript i refers to the growth species: n_i is the numerical density, m_i the mass, α_i the sticking coefficient, and the sum of all contributions β has the meaning of a flux of particles. The subscript $*$ refers to critical clusters: A_{N_*} is the surface area and a_0 is the radius of a monomer in the SiC lattice. Z is the Zeldovich factor (see Section 2 of Gail et al. 1984 for a detailed explanation).

Once J_*^S is computed for the conditions prevailing at each radius, the temporal evolution of the nucleation rate J_* is obtained from J_*^S just considering a time lag τ_* (see Gail et al. 1984)

$$\frac{\partial}{\partial t}\left\{ \frac{J_*}{\beta A_{N_*}} \right\} = -\frac{1}{\tau_*}\left\{ \frac{J_* - J_*^S}{\beta A_{N_*}} \right\} \tag{A4}$$

(2) The growth of grains occur by addition of species that incorporate into the grain, resulting in a temporal evolution for the grain radius a_{gr} of

$$\frac{\partial a_{gr}}{\partial t} = \sum_i^{N_0} \alpha_i \times \left(\frac{kT_k}{2\pi m_i}\right)^{1/2} \times (4\pi a_{gr}^2) \times n_i \times \frac{a_{0,i}}{3N_i^{2/3}} \tag{A5}$$

where the sum extends to all gaseous species i that produces growth of grains (here only SiC molecules are considered). The parameters α_i and m_i have the same meaning as in equation A3, $a_{0,i}$ is the radius of the species i in the lattice and N_i is the number of monomers of type i forming part of a grain.

The unknown parameters, such as the sticking coefficients and the form of the function θ_N for low N are chosen for obtaining an abundance and size of SiC grains in agreement with the literature: abundance relative to H_2 of $\sim 10^{-14}$ and radius of ~ 0.1 μm (Knapp 1985; Lorenz-Martins & Lefèvre 1993).

VISUAL EXTINCTION RADIAL PROFILE

The parameters A_i and C_i in equation 8 are usually given in the literature for plane-parallel geometry. Therefore, the evaluation of the photodissociation rate Γ_i of a species i through equation 8 is only valid for a species situated at point P in a plane-parallel layer (see Fig. B1), where the visual extinction measured along the direction perpendicular to the infinite plane is A_v^{pp}. But we want to know Γ_i at the different points r in spherical geometry. The strategy, then, is to find expressions for the UV field ($4\pi J_{UV}$) at points P and r in plane-parallel and spherical geometries respectively. Equaling both expressions we will determine the associated A_v^{pp}, that we will insert in equation 8.
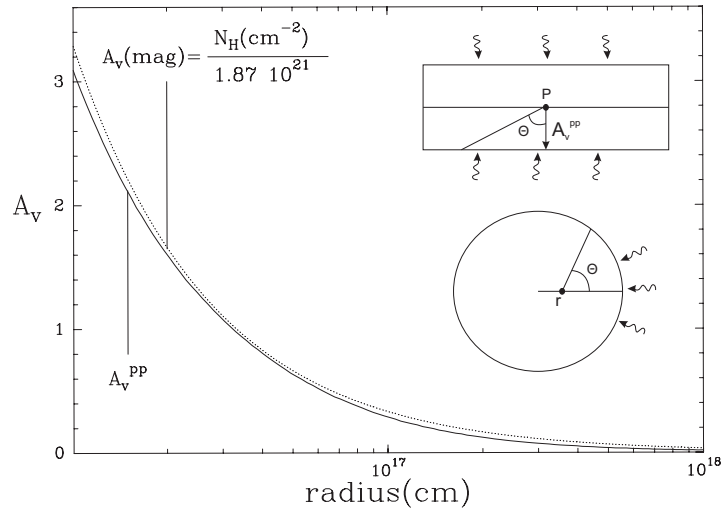

FIG. B1.— A_v radial profiles obtained from the plane-parallel to spherical correction (A_v^{pp}) and from the standard relation $A_v \propto N_H$ of Bohlin et al. (1978). The inserts show a two dimensions scheme of plane-parallel and spherical geometries.

The UV field at point P in a constant density plane-parallel layer is given by

$$4\pi J_{UV}(P) = 2\pi G_0 \int_0^\pi sin\theta exp\left\{ -\tau_{1000}(\theta) \right\} d\theta \quad , \quad \left[\tau_{1000}(\theta) = \left(\frac{\tau_{1000}}{\tau_{5500}}\right)\frac{A_v^{pp}}{1.086}\frac{1}{cos\theta} \right] \tag{B1}$$

where G_0 is the wavelength integrated specific intensity of the interstellar standard UV field (Draine 1978) (i.e. in photons cm^{-2} s^{-1} sr^{-1}), θ is the angle of the considered direction with respect to the normal to the surface. The UV opacity τ_{1000} has been expressed as a function of the visual extinction A_v^{pp} through the ratio of UV–to–visible opacities (τ_{1000}/τ_{5500}), where the subscript stands for the mean wavelength in $\mathring{A}$.

The UV field at point r within a sphere with a r^{-2} density law is

$$4\pi J_{UV}(r) = 2\pi G_0 \int_0^\pi sin\theta exp\big\{ - \tau_{1000}(r,\theta)\big\}d\theta \quad , \quad \left[\tau_{1000}(r,\theta) = \frac{\tau_{1000}^* r^*}{r\sqrt{1+cos^2\theta}}\Big\{\frac{\pi}{2} - atan\big(\frac{-cos\theta}{\sqrt{1+cos^2\theta}}\big)\Big\}\right] \quad \text{(B2)}$$

where it is necessary a boundary condition, e.g. the UV optical depth τ_{1000}^* at point r^* along the radial direction.

We have assumed $\tau_{1000}(r=10^{16})=12.7$ (Doty & Leung 1998), although the opacity at UV wavelengths is highly uncertain for IRC+10216, and a (τ_{1000}/τ_{5500}) ratio of 3.1 as measured by Rouleau & Martin (1991) for amorphous carbon grains of 0.05 μm, although different values up to 8 can be found in the literature depending on grain nature and size. The radial profile $A_v(r)$ obtained is shown in Fig. B1 where it is compared to the standard relation $A_v \propto N_H$ found for the interstellar medium by Bohlin et al. (1978). The interstellar UV field G has been decreased by a factor 2 with respect to the standard G_0 to make the abundance distributions of C$_2$H and CN (photodissociation products of C$_2$H$_2$ and HCN respectively) to peak at $\sim$15" and $\sim$20" respectively in agreement with interferometric observations (Dayal & Bieging 1995; Guélin et al. 1999). For our assumed distance of the star (150 pc) C$_2$H peaks at 3.4×10^{16} cm and CN at 4.5×10^{16} cm (see Fig. 5). We point out that this procedure is affected by a degeneracy between at least two parameters: the star distance, which transforms radial distances to angular distances, and the UV field and/or the A_v radial profile, which make molecules photodissociate at a shorter or larger radial distance. Despite the uncertainties in the knowledge of these quantities, and even if our assumption of a less intense UV field than the standard is not correct, the abundances of the different molecules will be predicted at the right angular positions.

REFERENCES

Allende Prieto, C., Lambert, D., L., & Asplund, M. 2001, ApJ, 556, L63

Apponi, A., J., McCarthy, M., C. et al. 1999, ApJ, 516, L103

Avery, L., W., Bell, M., B., et al. 1994, ApJ, 426, 737

Bagnulo, S., Doyle, J., G., & Griffin, I., P. 1995, A&A, 301, 501

Bell, M., B., Feldman, P., A., et al. 1982, Nature, 295, 389

Bell, M., B., Avery, L., W., & Feldman, P., A. 1993, ApJ., 417, L37

Bohlin, R., C., Savage, B., D., & Drake, J., F. 1978, ApJ, 224, 132

Bowen, G. H. 1988, ApJ, 329, 299

Bowers, P., F., & Knapp, G., R. 1987, ApJ, 315, 305

Boyle, R., J., Keady, J., J., et al. 1994, ApJ, 420, 863

Brownsword, R., A., Sims, I., R., et al. 1997, ApJ, 485, 195

Cernicharo, J., Kahane, C., et al. 1986, A&A, 164, L1

Cernicharo, J., Guélin, M., et al. 1987, A&A, 181, L9

Cernicharo, J., Gottlieb, C., A., et al. 1989, ApJ, 341, L25

Cernicharo, J., Guélin, M., et al. 1991, A&A, 246, 213

Cernicharo, J., Barlow, M., J., et al. 1996, A&A, 315, L201

Cernicharo, J., & Guélin, M. 1996, A&A, 309, L27

Cernicharo, J., Yamamura, I., et al. 1999, ApJ, 526, L41

Cernicharo, J., Guélin, M., & Kahane, C. 2000, A&AS, 142, 181

Cernicharo, J., Heras, A., M., et al. 2001, ApJ, 546, L123

Cernicharo, J., 2004, ApJ, 608, L41

Cernicharo, J., Pardo, J., R., et al. 2006, in preparation

Cherchneff, I., Barker, J., R., & Tielens, A., G., G., M. 1992, ApJ, 401, 269

Clary, D., C., Buonomo, E., et al. 2002, J. Phys. Chem. A, 23, 5541

Cox, A., N. 2000, Allen's Astrophysical Quantities, 4th ed., New York: AIP

Crosas, M., & Menten, K., M. 1997, ApJ, 483, 913

Dayal, A., & Bieging, J., H. 1995, ApJ, 439, 996

Doty, S. D., & Leung, C. M. 1998, ApJ, 502, 898

Draine, B., T. 1978, ApJS, 36, 595

Draine, B., T. 1979, Ap&SS, 65, 313

Fonfría, J., P., Cernicharo, J., et al. 2005, in preparation

Ford, K., E., S., & Neufeld, D., A. 2001, ApJ, 557, L113

Ford, K., E., S., Neufeld, D., A., et al. 2003, ApJ, 589, 430

Ford, K., E., S., Neufeld, D., A., et al. 2004, ApJ, 614, 990

Frenklach, M., Carmer, C. S., & Feigelson, E. D. 1989, Nature, 339, 196

Gail, H.-P., Keller, R., & Sedlmayr, E. 1984, A&A, 133, 320

Gensheimer, P., D., Likkel, L., & Snyder, L., E. 1995, ApJ, 439, 445

Glassgold, A., E., Lucas, R., & Omont, A. 1986, A&A, 157, 35

Glassgold, A., E. 1996, ARA&A, 34, 241

Goldhaber, D., M., Betz, A., L., & Ottusch, J., J. 1987, ApJ, 314, 356

González-Alfonso, E., & Cernicharo, J. 1993, A&A, 279, 506

Green, S. 1991, ApJS, 76, 979

Green, S. 1993, ApJS, 85, 181

Guélin, M., & Thaddeus, P. 1977, ApJ, 212, L81

Guélin, M., Green, S., & Thaddeus, P. 1978, ApJ, 224, L27

Guélin, M., Cernicharo, J., et al. 1987a, A&A, 175, L5

Guélin, M., Cernicharo, J., et al. 1987b, A&A, 182, L37

Guélin, M., Cernicharo, J., et al. 1997, A&A, 317, L1

Guélin, M., Neininger, N., & Cernicharo, J. 1998, A&A, 335, L1

Guélin, M., Neininger, N., et al. 1999, in The Physics and Chemistry of the Interstellar Medium, ed. V. Ossenkopf (Herdecke: GCA), 326

Hasegawa, T., I., Kwok, S., et al. 2006, ApJ, 637, 791

Henkel, C., Matthews, H., E., et al. 1985, A&A, 147, 143

Herbst, E., DeFrees, D., J., & Koch, W. 1989, MNRAS, 237, 1057

Herpin, F., & Cernicharo, J., 2000, ApJ, 530, L129

Keady, J., J., & Ridgway, S., T. 1993, ApJ, 406, 199

Knapp, G., R. 1985, ApJ, 293, 273

Konnov, A., A. 2000, http://homepages.vub.ac.be~akonnov/

Kwan, J., & Linke, R., A. 1982, ApJ, 254, 587

Le Teuff, Y. H., Millar, T., J., & Marckwick, A., J. 2000, A&AS, 146, 157

Lorenz-Martins, S., & Lefèvre, J. 1993, A&A, 280, 567

Lucas, R., & Guélin, M. 1990, in Submillimetre Astronomy, ed. G. D. Watt & A. S. Webster (Dordrecht: Kluwer), 97

Mamon, G. A., Glassgold, A. E., & Huggins, P., J. 1988, ApJ, 328, 797

McCabe, E., M. 1982, MNRAS, 200, 71

Meier, R., Eberhardt, et al. 1993, A&A, 277, 677

Melnick, G. J., Neufeld, D. A., et al. 2001, Nature, 412, 160

Millar, T., J., & Herbst, E. 1994, A&A, 288, 561

Moneti, A., Cernicharo, J., & Pardo, J., R. 2001, ApJ, 549, L203

Morris, M., Zuckerman, B., et al. 1971, ApJ, 170, L109

Morris, M., Gilmore, W., et al. 1975, ApJ, 199, L47

Morris, M., Turner, B., E., et al. 1976, ApJ, 205, 82

Moses, J., I., Bézard, B., et al. 2000, Icarus, 143, 244

Murrell, J., N., & Rodriguez, J., A. 1986, J. Mol. Struct. Theochem, 139, 267

Neufeld, D., A., Kaufman, M., J., et al. 2002, ApJ, 580, 278

Ohishi, M., Kaifu, N., et al. 1989, ApJ, 345, L83

Ridgway, S., T., & Keady, J. J. 1988, ApJ, 326, 843

Roberts, H., & Herbst, E. 2002, A&A, 395, 233

Rodgers, S., D., & Charnley, S., B. 2002, Planet. Space Sci., 50, 1215

Rouleau, F., & Martin, P., G. 1991, ApJ, 377, 526

Schutte, W., A., van der Hucht, K., A., et al. 1998, A&A, 337, 261

Smith, G., P., Golden, D., M., et al., 1999, GRI-Mech Version 3.0, http://www.me.berkeley.edu/gri_mech/

Smith, I., W., M., Herbst, E., & Chang, Q. 2004, MNRAS, 350, 323

Spaans, M., Neufeld, D., A., et al. 1998, ApJ, 503, 780
Thaddeus, P., Cummins, S., E., & Linke, R., A. 1984, ApJ, 283, L45
Thaddeus, P., Gottlieb, C., A., et al. 1985, ApJ, 294, L49
Tsuji, T. 1973, A&A, 23, 411
Tsuji, T. 2000, in The Carbon Star Phenomenon, ed. R. F. Wing (Dordrecht: Kluwer), 313
Tucker, K., D., Kutner, M., L., & Thaddeus, P. 1974, ApJ, 193, L115
Wang, S., Di Ventra, M., et al. 2001, Phys Rev Lett, 86, 5946

Wiedemann, G., R., Hinkle, K., H., et al. 1991, ApJ, 382, 321
Willacy, K., & Cherchneff, I. 1998, A&A, 330, 676
Willacy, K. 2004, ApJ, 600, L87
Wilson, R., W., Solomon, P., M., et al. 1971, ApJ, 169, L35
Winnewisser, G., & Walmsley, C., M. 1978, A&A, 70, L37
Witteborn, F., C., Strecker, D., W., et al. 1980, ApJ, 238, 577
Yamamoto, S., Saito, S., et al. 1987, ApJ, 323, L149